

Article

Magmatic–Hydrothermal Origin of Fe–Mn Deposits in the Lesser Khingan Range (Russian Far East): Petrographic, Mineralogical and Geochemical Evidence

Nikolai Berdnikov ¹, Pavel Kepezhinskas ^{1,*}, Victor Nevstruev ¹, Valeria Krutikova ¹, Natalia Konovalova ¹ and Valery Savatenkov ²

¹ Institute of Tectonics and Geophysics, Khabarovsk 680000, Russia; nick@itig.as.khb.ru (N.B.); nevstruevvg@mail.ru (V.N.); nm32697@gmail.com (V.K.); turtle_83@mail.ru (N.K.)

² Institute of Precambrian Geology and Geochronology, St. Petersburg 199034, Russia; v.m.savatenkov@ipgg.ru

* Correspondence: pavel_k7@yahoo.com

Abstract: Iron and iron–manganese deposits form three closely spaced clusters within the Lesser Khingan Range of the Russian Far East. Fe–Mn mineralization is hosted in Vendian–Cambrian carbonates and composed of magnetite, hematite, braunite, haussmanite, rhodochrosite and pyrolusite. The iron–manganese ores are closely associated with explosive intermediate–felsic breccias, magnetite-rich lavas, dolerites and mineralized lithocrystalloclastic tuffs. Magmatic rocks display both concordant and discordant relationships with Fe–Mn mineralization and contain abundant xenoliths of host carbonates. Both magmatic rocks (with the exception of Nb-enriched dolerites) and Fe–Mn ores are characterized by variable enrichments in large-ion lithophile and light rare earth elements and strong depletions in high-field strength elements compatible with the broad subduction setting for explosive volcanism and associated hydrothermal Fe–Mn ore mineralization. Nd–Sr isotope systematics suggest contamination by both ancient and juvenile continental crust and the involvement of recycled pelagic sediment in the formation of Fe–Mn deposits in the Lesser Khingan Range of the Russian Far East.

Keywords: Fe–Mn deposits; Russian Far East; Lesser Khingan Range; magmatic-hydrothermal; explosive breccia; magnetite lava; crustal contamination; subduction setting



Citation: Berdnikov, N.; Kepezhinskas, P.; Nevstruev, V.; Krutikova, V.; Konovalova, N.; Savatenkov, V. Magmatic–Hydrothermal Origin of Fe–Mn Deposits in the Lesser Khingan Range (Russian Far East): Petrographic, Mineralogical and Geochemical Evidence. *Minerals* **2023**, *13*, 1366. <https://doi.org/10.3390/min13111366>

Academic Editors: Xiaowen Huang and Xinfu Zhao

Received: 21 September 2023

Revised: 19 October 2023

Accepted: 24 October 2023

Published: 26 October 2023



Copyright: © 2023 by the authors. Licensee MDPI, Basel, Switzerland. This article is an open access article distributed under the terms and conditions of the Creative Commons Attribution (CC BY) license (<https://creativecommons.org/licenses/by/4.0/>).

1. Introduction

Iron and iron–manganese deposits in orogenic belts of different ages contain substantial resources of these important industrial metals and include different genetic types such as iron oxide–copper–gold (IOCG), Kiruna-type iron oxide–apatite (IOA; apatite–magnetite), sedimentary exhalative, magmatic–hydrothermal, volcanogenic (Cuban-type) and skarn-type deposits, as well as many other subtypes of Fe–Mn mineralization [1–30]. These “orogenic” deposits experienced variable scale contributions from a wide range of magmatic, hydrothermal, sedimentary and biological sources and processes [9,14,15,17,25,29,31–43]. A separate group of skarn-style magnetite mineralization (Cornwall-type deposits) has been documented in Pennsylvania and North China cratons in relation to interactions between basaltic magma, ore-forming fluids and host shale, sandstone and carbonate [44–46]. Many individual Fe- and Fe–Mn deposits and large Fe–Mn metallogenic belts are related to mafic-to-silicic explosive volcanism or contain detectable (substantial) volcanic components, as average global oceanic fluxes in dissolved iron and manganese from volcanic sources are estimated to be between 50 and 500 (median 180) and 0.6 and 3.2 (median 1.3) Gmol/year Fe and Mn, respectively [42]. Iron–manganese mineralization frequently occurs in young volcanic arcs (Aegean, Izu–Bonin–Mariana, Tonga–Kermadec, Vanuatu, New Britain, Kurile, Aleutian) and Cenozoic back-arc basins (Tyrrhenian Sea, Lau Basin, North Fiji Basin, Mariana Trough, Okinawa Trough; Sea of Japan, Sea of Okhotsk), [47–59] suggesting causal

links between active volcanism (frequently explosive), hydrothermal activity (hydrothermal mounds, hot springs, etc.) and iron–manganese mineralization in modern and ancient subduction zones [6,10–12].

The Lesser Khingan Range (LKR) forms a part of the Bureya–Jiamusi–Khanka (BJK) superterrane located at the southeastern end of the Central Asian Orogenic Belt (CAOB) [60–62]. The southern part of the LKR includes a cluster of Fe–Mn deposits, which form a 40 km wide mineralized belt extending from north to south across the state border into China [63]. Traditionally, these deposits were viewed as sedimentary or volcanogenic-sedimentary due to the stratiform appearance of constituting ore bodies and close association with Vendian–Cambrian sedimentary formations [64–66]. Iron resources in this Fe–Mn belt were estimated at 3 billion tons of iron ore [66], which makes them potentially comparable to the largest iron–manganese provinces in the Russian Federation [67]. An alternative view was pioneered by Berdnikov et al. [68], who proposed hydrothermal (probably with some hydrogenic component) origin for Fe–Mn mineralization in the LKR, possibly within a paleo-subduction magmatic–hydrothermal context. The magmatic–hydrothermal origin was further supported by the recognition of a close spatial and possibly genetic association between the Fe–Mn ores and explosive breccia (“fluidolites”), as the latter exhibit clear evidence of volcanic origin (ignimbrite-like textures, presence of altered volcanic glass and igneous minerals, etc.) along with the presence of platinum-group elements (PGE) and gold in both Fe–Mn ores and associated explosive breccia [69–75]. Platinum particles from the Poperechny Fe–Mn deposit (one of the largest ore bodies in the LKR cluster) were dated at 125 ± 21 Ma, indicating a Mesozoic volcanic overprint [72,73]. Explosive breccias in the Poperechny, Kaylan and Kostenga deposits are characterized by the large-ion lithophile element (LILE) and light rare earth element (LREE) enrichment, coupled with high-field-strength element (HFSE) depletion, suggesting that this Fe–Mn–PGE–Au overprint occurred in the paleo-subduction zone environment [72,74,75].

In this paper, we present new data on the mineralogy, petrology and geochemistry (including Sr–Nd isotopes) of Fe and Fe–Mn ores and associated volcanic rocks from three principal sites in the LKR metallogenic province, namely Poperechny, Kaylan and Kostenga deposits. We will then attempt to achieve the following goals using the data set specified above: (1) document occurrences of igneous rocks in association with iron–manganese mineralization (including their structural and textural relationships) and evaluate the possible role of magmatic (especially explosive) processes in the formation of the LKR Fe and Fe–Mn deposits; (2) determine the composition and model isotopic ages of mantle and crustal sources involved in the formation of these deposits in the LKR using new Nd–Sr data; (3) evaluate the relative roles of magmatic and hydrothermal processes during the formation of the LKR Fe and Fe–Mn deposits within the broad geodynamic setting of paleo-subduction of the Izanagi–Pacific plate beneath the Northeast Asian continent.

2. Geologic Background

The Bureya terrane forms a part of the complex Bureya–Jiamusi–Khanka superterrane at the southeast end of the CAOB (Figure 1).

This is usually viewed as a relic of Precambrian sub-continental blocks (typically together with the Khanka terrane) that were thermally, metamorphically and magmatically reworked during Paleozoic and Mesozoic within the tectonically evolving CAOB structure [76–80], or as a part of the Bureya–Jiamusi–Khanka superterrane, and is linked to the break-up of the Gondwana supercontinent and later-stage accretion of these continental fragments to the southeastern edge of Eurasia [81,82]. The Bureya terrane is composed of Neoproterozoic, Paleozoic and Mesozoic terrigenous and carbonate metasediments, along with various igneous rocks including gabbro, diverse granitoids, adakites and minor ultramafic rocks [75–80,83–85]. In essence, the Bureya terrane represents a large fragment of the Proterozoic accretionary prism metamorphosed under amphibolite-facies conditions during the Ordovician period [68,73,86].

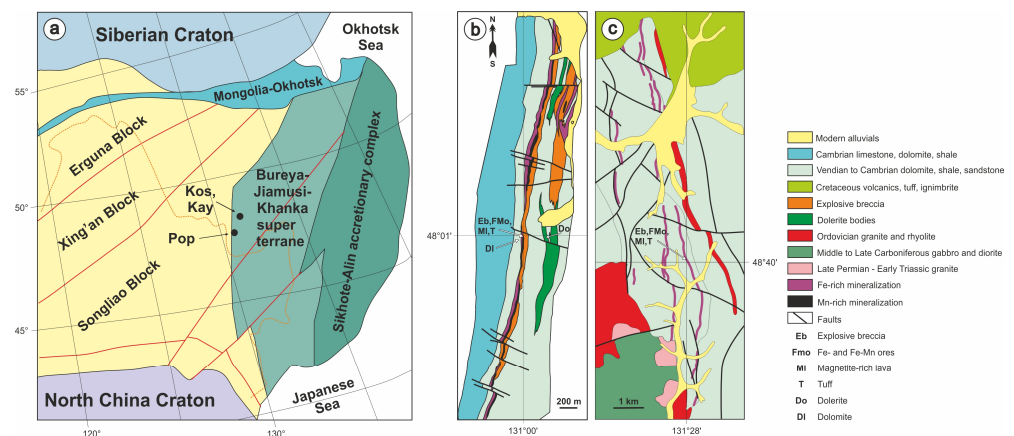


Figure 1. (a) Tectonic setting of the Poperechny (Pop), Kostenga (Kos) and Kaylan (Kay) iron–oxide deposits in the Russian Far East, modified after [75]. Orange dashed line depicts state border between China and Russian Federation. (b) Schematic geologic map of the Poperechny deposit, modified after [72]. (c) Schematic geologic map of the Kostenga deposit, modified after [74]. Sampling locations for various rock lithologies along designated key transects (exploration trenches) within the individual Fe–Mn deposits are marked by Eb (explosive breccia), FMo (Fe- and Fe–Mn ores), MI (magnetite-rich lava), T (tuff), Do (dolerite) and DI (dolomite). Other details of our field sampling procedures are provided in the text.

The iron and iron–manganese deposits and showings are localized within the sub-longitudinal zone of approximately 40 km wide, which stretches from the Amur river in the south to the Kimkan river over an approximate distance of 150 km [63,64,68]. Most of the individual sites are concentrated within three lateral clusters: (1) South Khingan with probably the best-explored Poperechny Fe–Mn deposit (9 million tons of ore at 21% Mn and 8%–34% Fe); (2) the Kimkan–Kostenga cluster with principal deposits of Kimkan, Kaylan and Kostenga (combined resources for the entire cluster are believed to be in excess of 600 million tons of ore [65,66]); (3) the Vostochny cluster, represented by a mid-size Bidzhan iron–manganese deposit (over 6 million tons of ore at 18.4% Mn and 13% Fe).

The Poperechny Fe–Mn deposit is hosted in the Vendian–Cambrian carbonates of the Murandavsky suite within the southern portion of the South Khingan cluster (Figure 1). Iron–manganese mineralization is represented by magnetite, hematite, braunite, hausmannite–braunite, braunite–hematite and rhodochrosite–hausmannite ores, along with their variably oxidized varieties [68,70–72]. Relatively unoxidized ore varieties typically contain around 20% Mn and 8% Fe, while oxidized and silicified ores may contain up to 35% of iron. Host Murandavsky suite limestones are partially dolomitized and intensely fractured coarse-grained sedimentary rocks with calcite, quartz and pyrite as typical fracture infill products. Murandavsky suite dolomites range from massive to locally sheared and are typically characterized by locally intense silicification and pyritization [68]. Volcanic rocks (tuffs, mineralized tuffs, explosive breccias) impregnate carbonate sediments and display both gradual transitions and discordant contacts with the Fe–Mn mineralization [70,72]. Abundant carbonate xenoliths in tuffs and explosive breccias, along with their discordant relationships with Vendian–Cambrian carbonates, are consistent with their later-stage formation, and probably contemporaneous with the iron–manganese ore [68,70–72].

The Kostenga Fe deposit is located in the central Kimkan–Kostenga cluster of iron–manganese mineralization. Similar to the Poperechny site, Kostenga mineralization is hosted by the Vendian–Cambrian Murandavsky carbonates, but Phanerozoic intrusive activity plays a significantly larger (both volumetrically and compositionally) role at Kostenga. Murandavsky dolomites at the southern terminus of the Kostenga deposit are intruded by the Ordovician granite, Middle to Late Carboniferous gabbro and Late Permian to Early Triassic granodiorite, while the ores and associated pyroclastics (“fluidolites”) are unconformably overlain by Cretaceous basalt–andesite–dacite–rhyolite volcanics [74]. Explosive

volcanic rocks associated with Fe mineralization at Kostenga, and are represented by andesitic breccias with abundant angular fragments of host carbonates and quartz–magnetite (occasionally with stilpnomelane, hematite and rare braunite) mineralization, along with lithocrystalloclastic tuffs, which frequently have ignimbrite-like textures [75]. Some iron ores from the Kostenga deposit display (as in the case of the Poperechny site) textural and mineralogical characteristics similar to the “magnetite lava” samples from the El Laco iron deposit in Northern Chile [31,35,40,87–89].

The Kaylan Fe deposit, just 10 km to the NE from the Kostenga site, appears to occupy a structurally and stratigraphically higher position, as iron–oxide mineralization is developed at the contact between Vendian–Cambrian dolomites and Lower Cambrian terrigenous–carbonaceous metasediments [68]. Magnetite ores seem to thin out towards the north, where the mineralization is overlain by Cretaceous felsic to intermediate lavas and tuffs. Magnetite–hematite ore lenses of from 0.2 to 2.4 m thick are intercalated with mineralized (predominantly magnetite) agglomerate tuffs, volcanic breccia, quartzite and massive hematite ore [75]. Similarly to the previously described deposits, phenocrysts and groundmass in some volcanic breccia are composed of magnetite, again resembling Fe-oxide volcanic rocks from the El Laco locality. Both explosive rocks and iron ore from the Kaylan deposit contain abundant fragments of the host carbonate, suggesting spatial and temporal proximity between the loci of volcanism and iron mineralization [75].

3. Analytical Methods

A total of more than 250 representative samples from the three key largest Fe and Fe–Mn deposits (Poperechny, Kostenga and Kaylan) in the LKR were analyzed in the course of this study by the various analytical methods summarized below. This study is based on an examination of 265 thin sections of sedimentary and volcanic rocks, along with Fe–Mn ores, XRF and ICP-MS determinations of major and trace elements in 212 samples (158 analyses were used to construct geochemical diagrams used in this study), and 148 photographs of hand specimens and polished sections of principal lithologies in the LKR Fe–Mn deposits (18 samples and polished sections used in this paper). Twenty-nine representative samples were analyzed in detail by the SEM-EDA.

Petrographic studies of Fe–Mn mineralization, along with igneous and sedimentary rocks, were carried out using an Imager A2m petrographic microscope (Carl Zeiss, Jena, Germany).

A detailed systematic study of mineral phases in ores and associated carbonates and volcanic rocks was completed using a VEGA 3 LMH TESCAN (Brno, Czech Republic) scanning electron microscope (SEM) with the Oxford X-Max 80 Gb energy dispersive spectrometer (EDS), with the following operating conditions: accelerating voltage of 20 kV, beam current of 530 nA and beam diameter of 0.2 μm . Reference samples including 37 natural and synthetic oxides, minerals and pure native metals (Oxford/108699 no. 6067) were used as standards. Co-standard Oxford/143100 no. 9864-15 was used for daily calibration of the SEM instrument. Accuracy of the EDS analyses was estimated to be ± 0.1 wt.%. Special sample preparation protocols, reported in detail in [68] and designed to prevent contamination, were utilized to expose metallic phases in situ and determine their relationships with host silicate and oxide phases, as well as associated rock-forming and accessory minerals.

Major elements were measured on pressed pellets using a S4 Pioneer XRF spectrometer (Bruker, Leipzig, Germany). International LDI-3 (gabbro) and WMG-1a (mineralized gabbro) reference materials were used for calibration. The analytical accuracy of major elements in the course of this study was $\pm 10\%$. Abundances of trace elements were determined with an ELAN 9000 ICP-MS (Perkin Elmer, Woodbridge, ON, Canada) after the acid digestion of a powdered sample. In addition to the standards listed above, geochemical reference samples BHVO-2 (USGS; Hawaiian basalt) and JB-3 (Geological Survey of Japan; Fuji basalt), along with Perkin Elmer standard solutions PE# N9300231-9300234 for internal calibration, were used to control the accuracy of analytical measurements. In the course of this study, the accuracy was $\pm 5\%$

for trace element abundances of >20 ppm and $\pm 10\%$ for chemical elements with abundances of <20 ppm. All the above-listed analytical procedures were carried out at the Khabarovsk Innovative-Analytical Center of the Institute of Tectonics and Geophysics, Far Eastern Branch of the Russian Academy of Sciences, Khabarovsk, Russian Federation. Additional details of sample treatment and analytical features can be found in [70,75].

Strontium and neodymium isotopes were measured using a Triton TI (Thermo Finnigan, Bremen, Germany), multi-collector, solid-phase mass spectrometry at the Institute of Precambrian Geology and Geochronology of the Russian Academy of Sciences, St. Petersburg, Russian Federation. Rb, Sr, Sm and Nd were extracted following the methods outlined in [90], and their elemental concentrations along with $^{87}\text{Rb}/^{86}\text{Sr}$ and $^{147}\text{Sm}/^{144}\text{Nd}$ isotope ratios were determined by isotopic dilution. Multiple runs of the BCR-1 reference sample were performed to determine analytical errors for Rb, Sr, Sm and Nd, which were estimated at $\pm 0.5\%$ for the course of this study. The total laboratory blank at the IPGG was 0.05 ng for Rb, 0.2 ng for Sr, 0.3 ng for Sm and 0.5 ng for Nd. Isotopic analysis reproducibility was controlled by the certified standards JNdi-1 ($^{143}\text{Nd}/^{144}\text{Nd} = 0.512117$) [91] and SRM-987 ($^{87}\text{Sr}/^{86}\text{Sr} = 0.710240$) [92]. The resulting $^{87}\text{Sr}/^{86}\text{Sr}$ value for SRM was 0.710275 ± 15 and the $^{143}\text{Nd}/^{144}\text{Nd}$ value for JNdi-1 was 0.512098 ± 9 for the period of this study. The Sr isotopic composition was normalized to $^{88}\text{Sr}/^{86}\text{Sr} = 8.37521$ and the Nd composition was normalized to $^{146}\text{Nd}/^{144}\text{Nd} = 0.7219$.

4. Results

Individual deposits in the LKR cluster include various sedimentary (dolomite, limestone, siltstone, mudstone) and volcanic (explosive breccia, tuff, tuffaceous siltstone, magnetite-rich lava) rocks, along with the associated Fe- and Fe-Mn mineralization. The following section presents the results of a petrographic, mineralogical and geochemical study of principal rock lithologies at the Poperechny, Kostenga, and Kaylan sites.

4.1. Petrography and Mineralogy

Mineralization in the LKR deposits (Figure 2a–d) is represented by massive and laminated ore composed of (in highly variable modal proportions) magnetite, hematite, limonite, goessite, braunite, haussmanite and rhodochrosite with subordinate (minor) pyrolusite, quartz, sericite, chlorite, gedritic–gruneritic amphibole, stilpnomelane, apatite, monazite, xenotime, La-Ce-Pr-Nd-oxides, pyrite and other sulfides. Ore is frequently saturated with fragments of tuffaceous pyroclastic material and intensely limonitized (Figure 2b–d). Lithocrystalloclastic and lithoclastic tuffs are variably mineralized (magnetite, hematite, rhodochrosite) and contain ash- to lapilli-sized (typically 0.5–1 mm to 20 mm in size, e.g., Figure 2e) fragments of host carbonates and Fe-Mn mineralization, along with ash-sized particles composed of quartz, dolomite, chlorite, biotite, amphibole, magnetite and sericite. Tuffs also form thin layers (from 1 to 15 mm) in stratified rocks composed of variable combinations of explosive breccia and iron-manganese ore (Figure 3d,f). Tephra fragments in mineralized tuffs are commonly angular, beveled and asymmetrical, with larger fragments being elongated up to 15–20 mm in length (Figure 3f). Mineralized tuffs are also frequently variably limonitized (Figure 2f,g). Explosive breccia (Figure 2h,i) is composed of large (1.5, rarely 10–20 cm in size) clasts imbedded in a fine-grained matrix, which occasionally contains strongly altered fragments of felsic (?) volcanic glass [72]. Breccia clasts account for 40%–60% of the total rock volume and are composed of various carbonates (predominantly dolomite and marble), Fe-Mn mineralization and previous (pre-breccia emplacement) generations of intermediate to felsic pyroclastic rocks including ignimbrite-like tephra with fiamme-like textures [72]. The groundmass of most explosive breccia samples is also characterized by ignimbrite-type fluidal textures [68,72]. Both carbonate and magmatic clasts are replaced with variable amounts of hematite, limonite, goethite and rhodochrosite [68]. Other secondary minerals and features in the explosive breccia include sericite, chlorite, secondary sulfides, quartz–chlorite and carbonate veinlets, as well as locally intense carbonatization, pyritization and silicification.

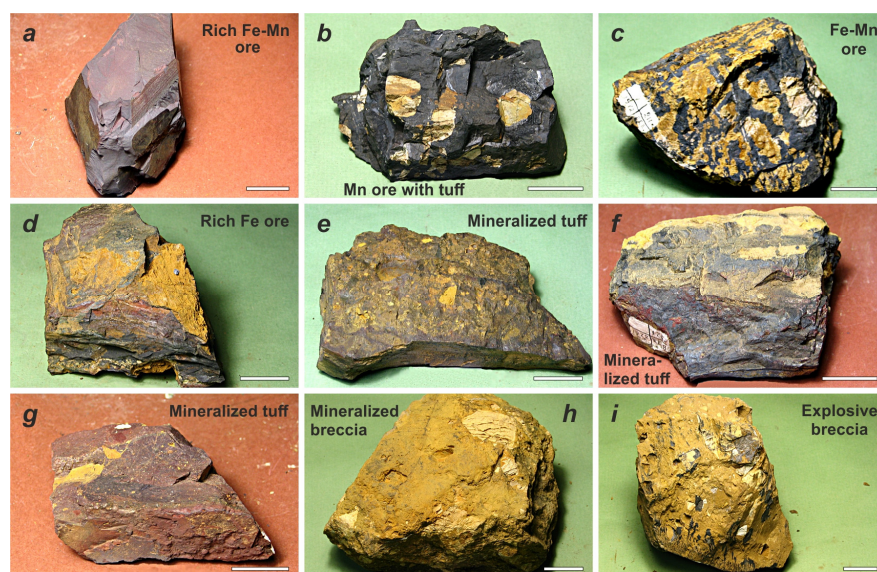


Figure 2. Photographs of iron and iron–manganese ores (a–d) and associated pyroclastic rocks (e–i) from the Lesser Khingan Range. Scale bar in all photographs is 2 cm.

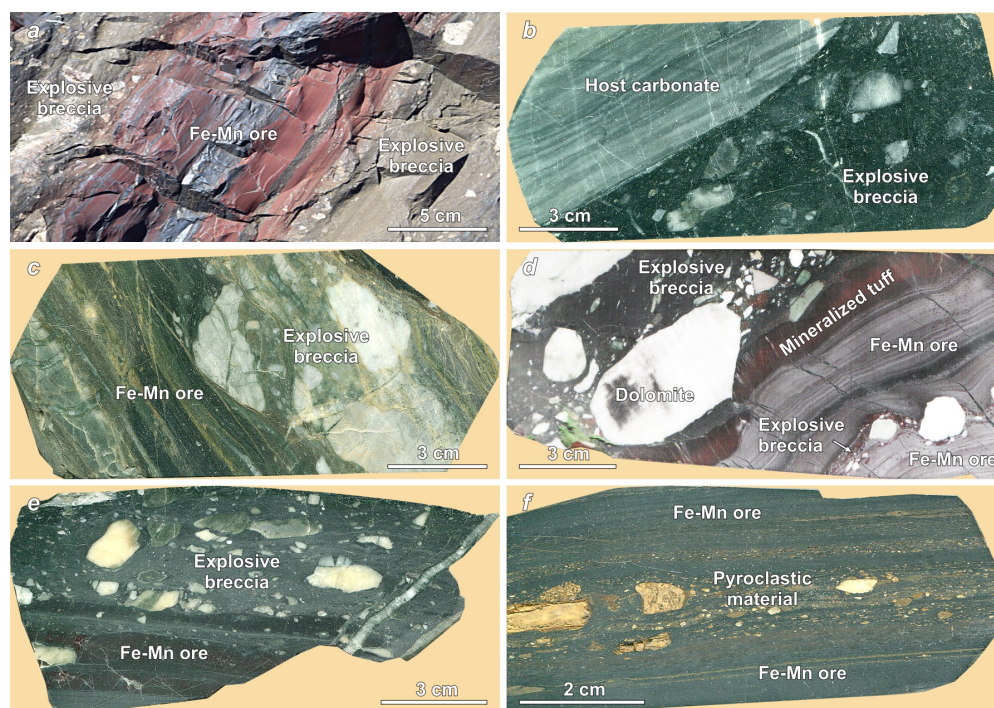


Figure 3. Relationships between explosive breccia, host carbonates and Fe-Mn mineralization. (a) Laminated Fe-Mn ore “sandwiched” between two layers of explosive breccia. (b) Discordant (extrusive) contact between explosive breccia and host carbonate. (c) Discordant (extrusive) contact between explosive breccia and Fe-Mn mineralization. (d) Layered cake structure of explosive breccia, mineralized tuff and Fe-Mn ore package. (e). Concordant contact between explosive breccia and Fe-Mn mineralization. (f) Fe-Mn ore interlayered with several bands rich in pyroclastic material. Note the difference between the size of pyroclastic material between the coarse main band in the middle of this sample and finer-grained satellite bands.

The geologic relationships between explosive breccia, host Vendian–Cambrian carbonates of the Murandavsky suite and Fe-Mn mineralization are illustrated in Figure 3. Explosive breccia frequently forms an interlayered sequence with laminated Fe and Fe-Mn

ores in all three LKR deposits (Kostenga, Kaylan, Poperechny) highlighted in the current study (Figure 3a). Locally, explosive breccia also displays clear discordant (extrusive) relationships with both the host carbonate (Figure 3b) and Fe-Mn mineralization (Figure 3c) suggesting later-stage injections of hot and fluidized felsic magma into the carbonate-Fe-Mn ore structural frame [68,72]. In most cases, however, locally explosive breccia has concordant contacts with the iron–manganese ore, which are sharp and devoid of any gradual transition features (Figure 3e). In some cases, explosive breccia forms laminated structures involving fine-grained tephra and Fe-Mn ore (Figure 3d), with pyroclastic rocks (both fine-grained mineralized tuff and explosive breccia) apparently filling the topographic irregularities (micro-relief lows) on the top of the fully consolidated Fe-Mn ore (Figure 3d). Also, locally, breccia-sized pyroclastic material alternates with ash-sized micro-layers (1–2 mm thick) within the massive-textured Fe-Mn mineralization (Figure 3f).

Microscopically, iron ores are represented by massive and laminated mineralization with crystalline to granular textures composed of magnetite, hematite, chlorite and quartz (Figure 4a). In addition, some feldspar (Figure 4a), monazite, apatite, sericite and amphibole (gedrite, ferrogedrite, grunerite) are observed in the Fe-ore from the Poperechny deposit [68,72]. Mineral abbreviations of all petrographic and mineralogical figures follow [93]. Explosive breccia typically contains angular fragments of dolomite and Fe-Mn mineralization, imbedded in a fine-grained matrix. The breccia matrix is characterized by an aphanitic to eutaxitic (Figure 4b) texture similar to the ones displayed by welded ignimbrite tuffs [94]. In addition to rock fragments, explosive breccia in the LKR Fe and Fe-Mn deposits contain variably shaped grains of quartz, amphibole, chlorite and sericite, along with unevenly distributed secondary Fe-oxides and hydroxides. The mineralized tuffs associated with Fe-Mn mineralization contain various lithic clasts and individual mineral grains in the fine-grained vitric matrix (Figure 4c,d). Some coarse-grained tuffs display a strong alignment of dolomitic clasts and magnetite grains in a non-welded ignimbrite-like matrix composed of magnetite, biotite and quartz (Figure 4c). Some crystalloclastic tuffs show variably deformed biotite laths (partially replaced with chlorite) imbedded in a magnetite–chlorite–feldspar–quartz matrix (Figure 4d). Magnetite-rich lava is represented by banded (Figure 4e) and massive (Figure 4f) porphyritic varieties with phenocrysts composed of equigranular magnetite, quartz and feldspar. Groundmass also occasionally contains biotite, amphibole, monazite, apatite and zircon, along with secondary chlorite, sericite, hematite and rhodochrosite. Banding, in some Fe-rich lavas, is emphasized by the strong alignment and orientation of magnetite aggregates, elongated carbonate fragments and light-colored feldspar-quartz bands (Figure 4e). Locally, magnetite-rich lavas are cross-cut by thin (<50 microns) secondary carbonate veinlets (Figure 4f). Basaltic intrusions associated with explosive breccia display typical ophitic (doleritic) textures composed of elongated prismatic clinopyroxene and plagioclase (Figure 4g). Dolerites also frequently contain large equant olivine phenocrysts (Figure 4h) and euhedral to subhedral late-stage amphibole grains (Figure 4g,h, respectively). Some host dolomites of the Vendian–Cambrian Murandavsky suite contain equant subhedral to anhedral olivine porphyroblasts (Figure 4i), most probably reflecting contact chemical changes due to the injection of hot intermediate to felsic magma into carbonate’s structural frame [68,72].

Iron–manganese mineralization includes some additional accessory mineral phases, as suggested by detailed SEM mineralogical studies. The quartz–hematite–magnetite ore contains anhedral grains and segregations of Fe-rich dolomite and Mg-rich siderite (Figure 5a). Magnetite–hematite–quartz, magnetite–hematite–quartz–chlorite and magnetite–hematite–quartz–chlorite–sericite varieties also frequently include euhedral to anhedral grains of apatite (Figure 5b) and monazite (Figure 5d) and xenotime (Figure 5e). Some hematite-rich iron ores contain precious metal minerals such as non-stoichiometric silver chloride (Figure 5c). One sample of hematite-quartz ore from the Poperechny deposit includes a single anhedral grain of Pb-Bi selenotelluride (Figure 5f). Selenotellurides of chalcophile metals are common ore mineral phases in the wide range of epithermal, porphyry, orogenic and intrusion-related gold (gold–telluride) deposits [95–99].

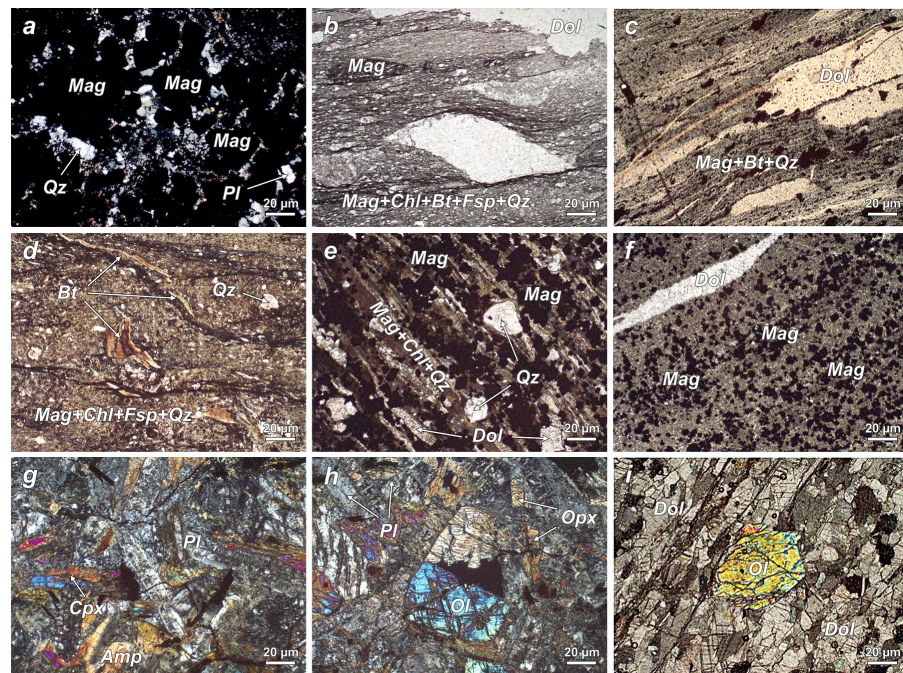


Figure 4. Photomicrographs of principal rock lithologies at the LKR deposits. (a) Iron-rich ore with massive texture. (b) Explosive breccia. (c) Lithocrystalloclastic tuff with strong alignment of predominantly dolomitic fragments. (d) Crystalloclastic tuff with banded and deformed biotite crystals partially replaced with chlorite. (e) Banded magnetite-rich lava. (f) Magnetite-rich lava with equant euhedral to subhedral magnetite microphenocrysts and carbonate veinlets. (g) Dolerite with doleritic texture composed of elongated clinopyroxene and plagioclase laths. (h) Euhedral olivine phenocryst in dolerite. (i) Porphyroblastic olivine in recrystallized dolomite. Mineral abbreviations here and in all other figures are as follows [93]: Mag—magnetite, Qz—quartz, Pl—plagioclase, Chl—chlorite, Bt—biotite, Fsp—feldspar, Dol—dolomite, Cpx—clinopyroxene, Amp—amphibole, Ol—olivine.

Magnetite-rich lavas from the Kostenga and Poperechny Fe-Mn deposits in the LKR carry euhedral to subhedral magnetite phenocrysts and microphenocrysts hosted in amphibole–biotite–quartz–monazite groundmass (Figure 6a,b). Some samples also contain metasomatic rhodochrosite (Figure 6a), and possibly some other secondary Fe-Mn mineral phases [68]. Relatively rare amphiboles in the LKR magnetite-rich lava are represented by minute ferrogedrite crystals (Figure 6a). Some Fe-rich lava samples from the Kostenga deposit display distinctive fragmentation, which locally turns into macro- to micro-scale layering or banding consisting of alternating magnetite, quartz–magnetite–apatite and quartz–biotite mineral bands (Figure 6c). Somewhat similar textural and mineral banding has previously been reported from the magnetite-rich El Laco lavas and some other Fe-rich volcanic localities in northern Chile [35,39,46,100]. Magnetite lavas at both Poperechny and Kostenga sites carry some silver (in addition to PGE and Au, described earlier in more detail [69–75]) mineralization represented by various Ag-bearing alloys, sulfides and halides (Figure 6d–f). Cupriferous silver, along with Cu–Ag–Au alloys [74,75,101], forms elongated euhedral particles in the rhodochrosite–quartz–biotite groundmass (Figure 6d), while anhedral acanthite is present in the chlorite–magnetite-dominated matrix (Figure 6e). Another rather remarkable silver mineral phase is represented by equant grains or aggregates of non-stoichiometric silver chloride associated with euhedral magnetite grains in a fine-grained chlorite–quartz–magnetite groundmass (Figure 6f). Non-stoichiometric silver chloride, along with acanthite and other silver-bearing sulfides, appears to be relatively common in Paleozoic black shale–volcanogenic formations, arc plutonic root complexes and Cenozoic volcanic rocks from a range of subduction- and non-subduction-related environments, where its origins are linked to the involvement of subduction-related hydrothermal fluids enriched in water, sulfur, and chlorine [99,102–104].

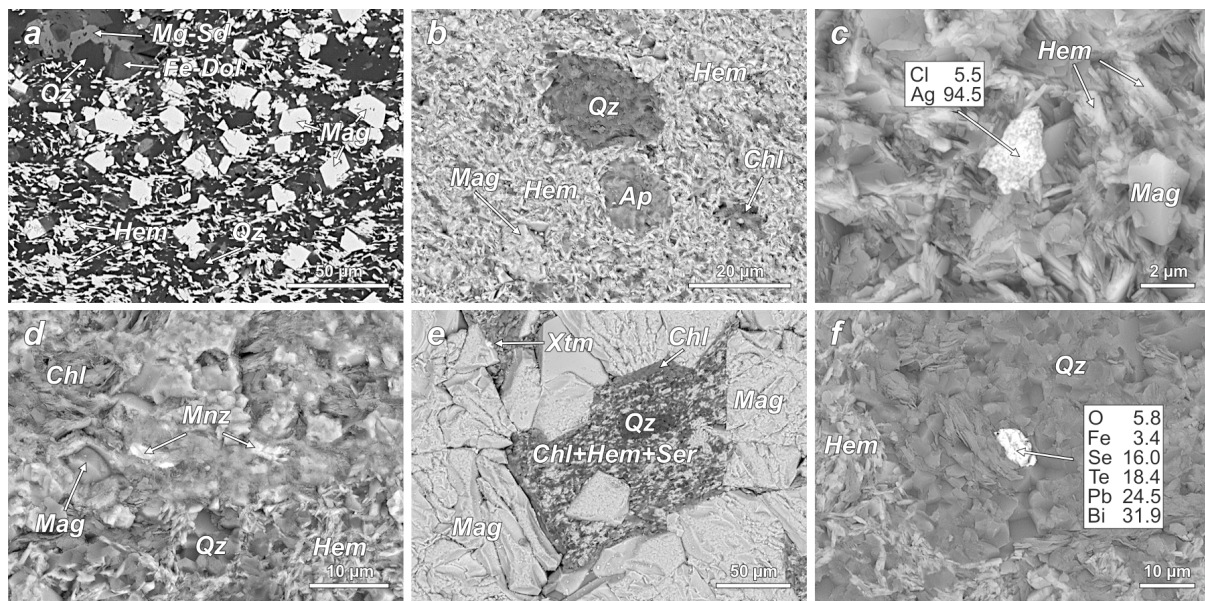


Figure 5. BSE images of Fe-Mn ores from the Poperechny Fe-Mn deposit (a,b). Fine-grained magnetite–hematite ore with quartz, apatite, chlorite, Fe-dolomite and Mg-siderite. (c) Micro-inclusion of non-stoichiometric silver chloride (chlorargyrite) in a very fine hematite–magnetite matrix. (d) Hematite–magnetite ore with quartz, chlorite and monazite. (e) Hematite–magnetite ore with quartz, chlorite, sericite and xenotime. (f) Micro-inclusion of lead–bismuth seleno–telluride in quartz in association with hematite. Here and in Figure 6, insert tables include results of the SEM-EDA analysis of relevant mineral phases in wt.%. Mag—magnetite, Hem—hematite, Chl—chlorite, Ser—sericite, Qz—quartz, Mnz—monazite, Xtm—xenotime, Fe-Dol—Fe-dolomite, Mg-Sd—Mg-siderite.

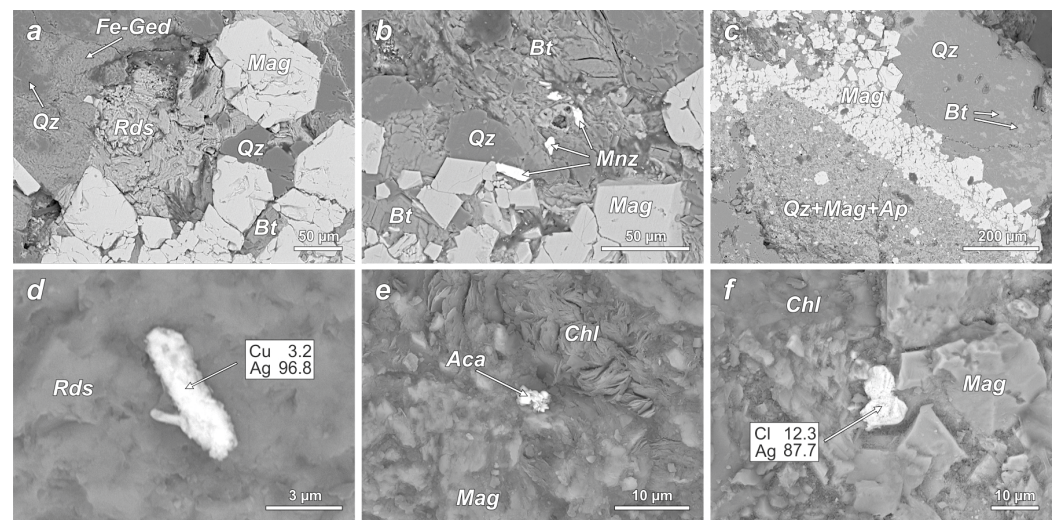


Figure 6. BSE images of magnetite-rich lavas from Kostenga (a–c) and Poperechny (d–f) deposits in the Lesser Khingan Range. (a,b) Porphyritic texture of magnetite-rich lava with magnetite phenocrysts and micro-phenocrysts in rhodochrosite–ferrogedrite–monazite–biotite–quartz groundmass. (c) Banded-like, or fragmentary, texture of magnetite lava with alternating magnetite, quartz–biotite and quartz–magnetite–apatite bands. (d) Micro-inclusion of cupriferous silver in the rhodochrosite-rich groundmass. (e) Micro-inclusion of acanthite in the chlorite–magnetite groundmass. (f) Micro-inclusion of non-stoichiometric silver chloride (chlorargyrite) in magnetite groundmass. Mag—magnetite, Bt—biotite, Chl—chlorite, Fe-Ged—ferrogedrite, Qz—quartz, Mnz—monazite, Rds—rhodochrosite, Aca—acanthite.

4.2. Geochemistry

The whole-rock geochemistry of explosive breccia and other mineralized pyroclastic rocks, along with various textural types of ore from the LKR deposits, was previously reported in [68–75]. Here, we list some representative whole-rock major and trace element analyses (Table 1) for the samples that were analyzed for Sr and Nd isotopes. In addition, in this section, we present major and trace element compositions of magnetite-rich lavas from the Poperechny and Kostenga deposits, which appear to play an integral role in the formation of iron–manganese deposits in the LKR (Table 2).

Table 1. Representative major and trace element compositions of principal rock lithologies associated with the Poperechny deposit.

Sample#	3-10	4-08	4-17	128-1	789	789-Д	117
Rock Type	Eb1	Eb2	Eb3	FMo	Do1	Do2	DI
SiO ₂ (wt.%)	59.49	61.79	55.44	39.20	51.83	50.22	12.29
TiO ₂	0.99	0.70	0.66	0.40	1.56	1.53	0.04
Al ₂ O ₃	13.64	12.74	10.71	2.62	10.41	10.24	0.40
Fe ₂ O ₃	7.86	3.70	5.71	24.21	10.66	11.32	1.58
MnO	0.18	0.05	0.14	14.95	0.13	0.13	0.15
MgO	4.75	4.21	6.09	6.38	10.88	11.46	17.95
CaO	2.11	4.46	6.58	2.08	4.70	4.59	31.87
Na ₂ O	2.44	0.19	0.28	0.88	5.51	5.00	0.00
K ₂ O	2.86	3.39	2.65	2.16	0.32	0.33	0.02
P ₂ O ₅	0.12	0.13	0.13	0.09	0.14	0.14	0.00
LOI	5.42	8.96	11.86	5.97	3.38	4.38	45.18
Total	99.85	100.33	100.25	98.95	99.52	99.35	109.48
Cr (ppm)	43.32	88.93	88.85	21.54	356.63	346.74	7.35
Ni	276.33	46.20	158.40	429.91	166.39	160.01	11.95
Co	12.57	9.59	29.90	419.43	45.57	43.85	1.45
V	75.67	177.39	162.93	83.75	134.24	132.69	5.73
Sc	16.08	10.96	10.81	6.73	17.96	17.95	0.36
Cs	4.49	7.28	6.41	18.65	2.54	2.83	0.09
Rb	100.08	126.59	102.26	127.68	8.10	9.15	1.04
Ba	1350.92	555.10	464.0	784.19	308.44	323.03	33.60
Sr	50.62	62.48	82.70	79.39	208.9	198.73	54.24
Zr	74.47	69.21	88.31	52.13	57.49	61.03	24.27
Y	14.31	15.10	16.73	11.51	15.37	16.11	1.39
Nb	4.82	3.28	3.20	7.43	9.92	9.94	1.05
Ta	0.40	0.24	0.32	0.23	0.84	0.80	<0.001
Hf	2.10	2.00	2.34	1.39	1.80	1.82	0.82
Th	8.31	6.58	6.39	2.81	0.68	0.63	0.43
U	0.64	1.46	1.90	0.81	0.21	0.22	0.05
La	33.29	23.46	23.74	10.45	6.11	6.17	1.10
Ce	69.73	50.09	51.09	25.27	13.81	13.58	2.08
Pr	7.63	5.66	5.76	2.76	1.84	1.89	0.28
Nd	31.02	24.16	24.63	10.67	8.73	8.78	1.19
Sm	6.11	4.72	4.79	2.25	2.67	2.72	0.25
Eu	0.99	0.93	0.96	0.48	1.02	1.05	0.07
Gd	5.75	4.56	4.65	2.60	3.57	3.59	0.29
Tb	0.65	0.52	0.55	0.39	0.56	0.57	0.03
Dy	3.47	2.95	3.16	2.39	3.19	3.26	0.19
Ho	0.59	0.55	0.60	0.51	0.60	0.61	0.04
Er	1.84	1.76	1.93	1.70	1.59	1.61	0.12
Tm	0.24	0.25	0.27	0.28	0.21	0.21	0.02
Yb	1.70	1.78	1.98	2.14	1.28	1.27	0.12
Lu	0.23	0.26	0.29	0.34	0.18	0.18	0.02
Ag (ppm)	0.65	1.36	0.55	0.14	0.16	0.24	0.16
Cu	45.69	47.29	47.32	6.07	51.53	38.26	14.54
Zn	103.55	64.48	103.94	59.86	127.97	131.43	18.17
Sn	2.80	2.36	1.75	0.80	1.17	0.82	<0.001
Sb	N.A.	N.A.	N.A.	0.38	N.A.	N.A.	0.01
Pb	4.54	5.31	14.18	11.74	2.33	0.92	0.27
Bi	N.A.	N.A.	N.A.	<0.001	N.A.	N.A.	1.32
As	N.A.	N.A.	N.A.	16.12	N.A.	N.A.	0.24

Note: N.A.—not analyzed. Eb—explosive breccia, FMo—Fe-Mn ore, Do—dolerite, DI—dolomite.

Table 2. Major and trace element compositions of magnetite-rich lavas from the LKR.

Deposit	Kostenga			Poperechny	
	Sample#	757	758-1	759	116
SiO ₂ (wt.%)	69.60	39.20	65.40	33.37	22.66
TiO ₂	0.22	0.49	0.11	0.26	0.25
Al ₂ O ₃	2.30	7.06	1.87	2.36	1.45
Fe ₂ O ₃	22.01	11.65	26.48	33.53	25.52
MnO	0.03	6.18	0.99	5.26	17.01
MgO	1.57	7.46	1.51	4.77	4.77
CaO	1.01	9.17	0.68	6.51	6.54
Na ₂ O	0.12	0.19	0.10	0.08	0.10
K ₂ O	0.32	1.37	0.37	0.05	0.04
P ₂ O ₅	0.75	0.11	0.32	0.04	0.05
S	0.01	0.00	0.01	N.A.	N.A.
F	0.55	0.11	0.66	N.A.	N.A.
LOI	1.58	17.56	1.48	12.50	22.05
Total	100.05	100.57	99.98	100.02	100.45
Cr (ppm)	61.94	53.52	22.84	12.77	9.92
Ni	14.28	54.77	37.11	70.45	61.17
Co	13.87	67.87	22.97	144.69	242.97
V	59.55	62.34	47.78	73.54	11.35
Sc	6.16	10.03	3.48	5.50	4.25
Cs	9.45	3.91	18.91	0.94	1.48
Rb	21.59	54.01	31.42	2.05	1.61
Ba	144.84	830.1	822.8	48.35	161.47
Sr	67.60	265.25	41.88	29.96	125.96
Zr	11.40	45.22	6.44	33.55	25.43
Y	11.63	10.02	4.82	6.95	8.16
Nb	2.83	8.65	1.38	5.07	3.48
Ta	0.07	0.55	0.03	0.09	0.04
Hf	<0.001	1.41	<0.001	0.77	0.42
Th	1.63	5.63	0.77	1.56	1.12
U	0.26	0.60	0.27	0.24	0.24
La	9.48	20.15	2.31	4.76	7.20
Ce	20.86	40.81	4.83	12.58	14.92
Pr	2.81	4.98	0.68	1.37	1.72
Nd	12.18	18.78	2.96	5.65	6.70
Sm	2.81	3.73	0.71	1.25	1.38
Eu	0.74	0.75	0.19	0.27	0.35
Gd	3.51	3.70	0.87	1.50	1.66
Tb	0.51	0.46	0.13	0.21	0.25
Dy	2.84	2.17	0.78	1.34	1.59
Ho	0.54	0.42	0.16	0.29	0.34
Er	1.45	1.28	0.52	0.99	1.12
Tm	0.20	0.21	0.08	0.15	0.18
Yb	1.29	1.45	0.57	1.05	1.21
Lu	0.19	0.24	0.10	0.16	0.19
Ag (ppm)	1.45	1.12	2.44	0.07	0.01
Cu	11.82	17.99	<0.001	6.01	6.13
Zn	2.74	69.83	32.89	24.45	15.90
Sn	<0.001	1.40	<0.001	0.62	0.31
Sb	0.74	0.38	0.31	0.08	0.86
Pb	4.33	26.99	0.79	<0.001	5.30
Bi	0.05	0.23	0.04	<0.001	0.12
As	1.46	13.35	1.23	0.27	1.33
Ir (ppb)	<0.001	<0.001	<0.001	1.75	2.89
Ru	<0.001	0.30	<0.001	0.49	1.88
Rh	<0.001	<0.001	<0.001	0.17	1.68
Pt	4.34	5.91	5.60	2.77	2.95
Pd	<0.001	<0.001	<0.001	3.42	97.11
Au	1335.6	289.96	1351.61	301.45	38.85

Note: N.A.—not analyzed.

Major element variations in explosive breccia and mineralized tuffs from the LKR iron and iron–manganese deposits identify them as strongly differentiated volcanic rock series. Pyroclastic rocks plot into the fields of picrite, picrobasalt, basaltic andesite, andesite, dacite and rhyolite on the TAS diagram [105], with individual analyses plotting into basanite, trachybasalt, basaltic trachyandesite and even tephrite compositional fields (Figure 7a). This evident dichotomy regarding the alkalis is further emphasized by the K_2O – SiO_2 relationships (Figure 7b), where most of the Kaylan volcanic rocks plot into the low-K tholeiitic and calc-alkaline fields of Peccerillo and Taylor [106], while magmatic samples from the Poperechny, and especially Kostenga, deposits populate the high-K calc-alkaline and shoshonitic compositional fields (Figure 7b). Interestingly enough, a few individual samples from all three deposits plot into all compositional fields (tholeiitic, calc-alkaline, high-K calc-alkaline, shoshonitic) on the K_2O – SiO_2 diagram (Figure 7b), possibly suggesting that different magma batches with respect to potassium content participated in the formation of Fe–Mn deposits in the LKR.

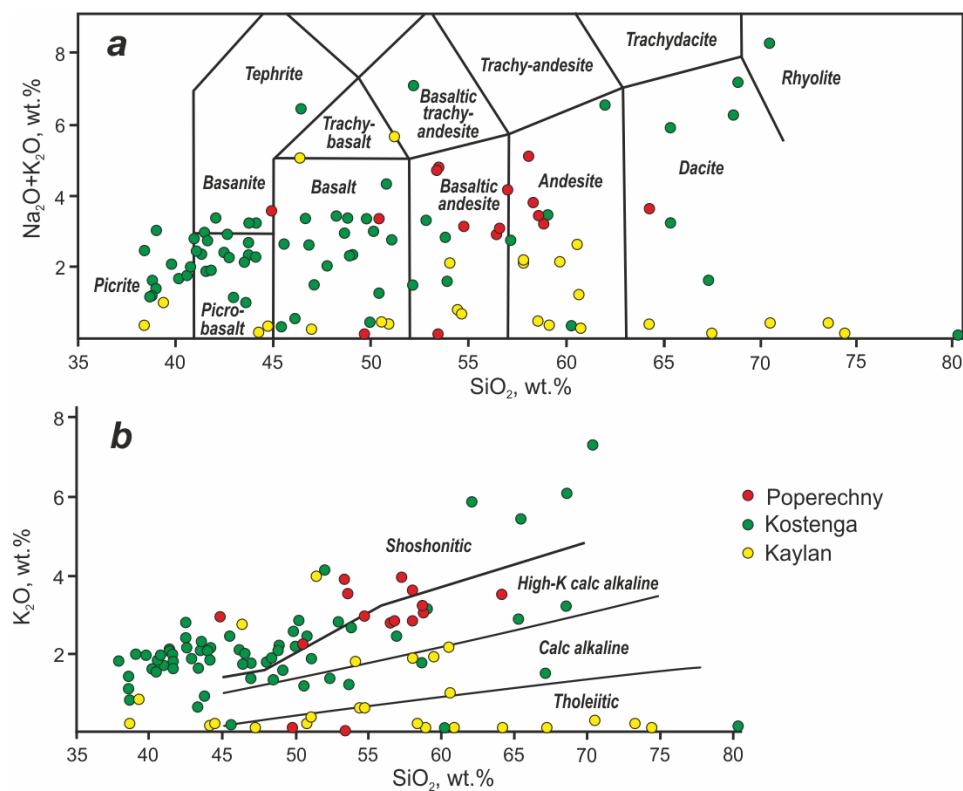


Figure 7. Major element variations in the volcanic rocks from the Poperechny, Kostenga and Kaylan deposits in the Lesser Khingan Range. (a) Total alkali–silica (TAS) diagram. Compositional fields are from [105]. (b) K_2O versus SiO_2 classification diagram for tholeiitic, calc–alkaline and shoshonitic volcanic rock series after [106].

Trace element variations in explosive breccia, mineralized tuffs and Fe–Mn ores from the LKR deposits normalized to primitive mantle [107] are summarized in Figure 8. Explosive breccia from all three deposits under consideration (Poperechny, Kostenga, Kaylan) is characterized by a general enrichment in large-ion lithophile elements (LILE). Ba and Rb contents in Kostenga and Kaylan deposits exhibit significant variations, with Ba being depleted in Kostenga and Rb in Kaylan explosive breccia, while Cs is uniformly enriched in all three LKR deposits. High-field strength elements (HFSE), such as Nb, Ta, Zr and Hf, are depleted in all explosive breccia samples from the LKR with respect to LILE and light rare-earth elements (LREE) (Figure 8a,d,g). Explosive breccia is also characterized by the moderate enrichment of LREE to the heavy rare-earth elements (HREE) typical of most subduction-related volcanic rocks [108,109]. All analyzed explosive breccia samples

also exhibit prominent negative Sr anomalies. Mineralized tuffs from the Poperechny and Kaylan deposits contain highly variable amounts of LILE, coupled with alternating positive and negative Rb and Ba anomalies (Figure 8b,h), while Kostenga tuffs display negative Ba and prominent positive U anomalies that are almost identical to the U enrichments observed in explosive breccia from the Kostenga and Kaylan deposits (Figure 8d,g). All tuffs are characterized by distinct depletions in HFSE (Nb, Ta, Zr and Hf) on primitive mantle normalized trace element patterns, and weak to moderate LREE enrichments over HREE (Figure 8b,e,h), which are broadly similar to the LKR explosive breccia (Figure 8a,d,g). Iron and iron-manganese ore from the Poperechny and Kostenga deposits display a general enrichment of LILE and LREE with respect to HFSE and HREE (Figure 8c,f). Mineralization in Kostenga is also characterized by prominent positive U and negative Sr anomalies (Figure 8f) similar to those observed in many pyroclastic rocks from the LKR (Figure 8d,e,g,h). Ores from the Kaylan deposit are characterized by the most fractionated primitive-mantle normalized trace element compositions, with depletions in Cs, Rb, U, Ta, Hf and HREE (Yb and Lu), coupled with strong enrichments in Ba, Nb, Sr and Y. In general, with the exception of the Kaylan ore, volcanic rocks (explosive breccias and mineralized tuffs) appear to share trace element characteristics with the iron–manganese mineralization.

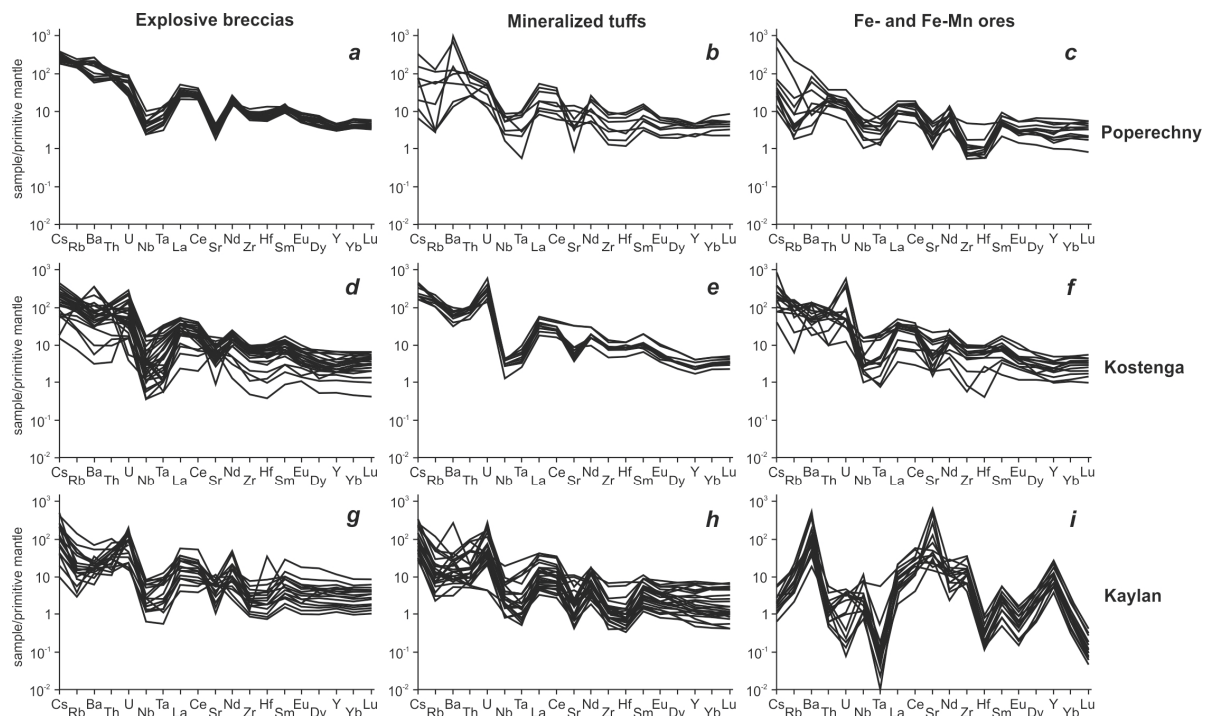


Figure 8. Incompatible trace element variations in explosive breccias (a,d,g), mineralized tuffs (b,e,h) and ores (c,f,i) from the Poperechny, Kostenga and Kaylan iron–manganese deposits in the Lesser Khingan Range. Normalizing values for primitive mantle are from [107].

Magnetite-rich lavas from the Kostenga and Poperechny Fe–Mn deposits are characterized by primitive mantle-normalized patterns with clear LILE enrichment compared to HFSE and HREE, emphasized by the pronounced negative anomalies of HFS elements such as Nb, Ta and Zr (Figure 9a). Some Fe-rich lava samples also share negative Sr anomalies with the LKR pyroclastic rocks (Figures 8 and 9); in other magnetite lava samples, the Sr anomaly is virtually absent. Rare earth element distribution in magnetite-rich lava is also comparable to the explosive volcanic rocks from Poperechny and Kostenga, displaying moderate LREE enrichment in reference to the HREE and a very weak, but still detectable, negative Eu anomaly (Figure 7b). In general, the trace element geochemistry of magnetite-rich lava from the Poperechny and Kostenga sites is broadly similar to other volcanic rocks from the same deposits in the LKR.

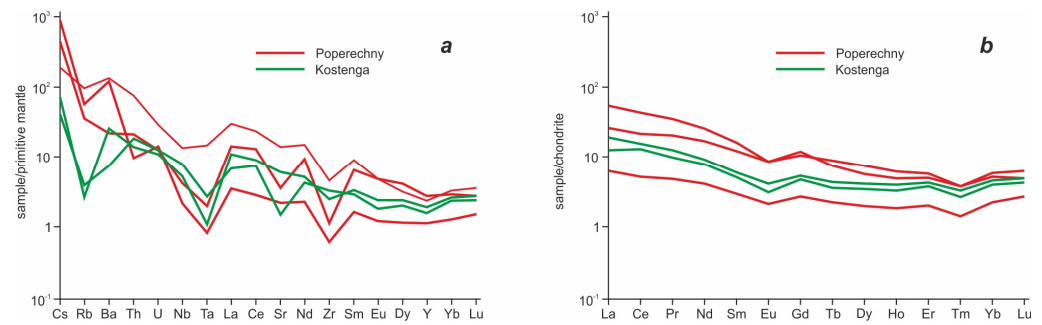


Figure 9. Incompatible trace (a) and rare earth (b) element variations in magnetite-rich lavas from the Kostenga and Poperechny iron–manganese deposits in the Lesser Khingan Range. Normalizing values for primitive mantle are from [107] and those of average chondrite are from [108].

Finally, the dolerite intrusions associated with explosive breccia at Poperechny exhibit trace element compositions that are enriched in HFSE (Nb = 9.92 and 9.94 ppm; Ta = 0.80 and 0.84 ppm; Table 1) and only slightly enriched in LREE compared to HREE (La/Sm = 2.28 and 2.26, La/Yb = 4.77 and 4.86, respectively, in samples Do1 and Do2; Table 1).

4.3. Sr and Nd Isotopes

The results of Sr and Nd isotope measurements in explosive breccia, host dolomite, Fe-Mn mineralization and dolerite from the Poperechny iron–manganese deposits are summarized in Table 3. The explosive breccia displays extremely variable initial ⁸⁷Sr/⁸⁶Sr ratios that range from 0.71277 to 0.74238, and uniformly low negative ε_{Nd}(t) values that range from −8.90 to −11.21 (Table 3). These Nd-Sr isotopic characteristics in the explosive breccia are coupled with La/Sm and La/Yb enrichments (4.95–5.44 and 12–19.58, respectively; Table 1). Host dolomite from the Murandavsky suite has a similar Nd-isotope composition to the volcanic breccia (ε_{Nd}(t) of −8.83) and a lower initial ⁸⁷Sr/⁸⁶Sr ratio of 0.70789 (Table 3). The Fe-Mn ore displays an initial ⁸⁷Sr/⁸⁶Sr isotope ratio of 0.72027, which is within the range of Sr-isotope values in the volcanic explosive breccia, and a more radiogenic isotope composition of neodymium ε_{Nd}(t)= −3.92 (Table 3). Finally, later-stage dolerite bodies, which cut both host dolomite and Fe-Mn mineralization, have a slightly depleted Nd-isotopic composition above CHUR values (ε_{Nd}(t) of 1.95 and 2.03), and relatively low initial ⁸⁷Sr/⁸⁶Sr isotopic ratios of 0.70851 and 0.70566, respectively (Table 3), suggesting that Nb-enriched dolerites (Nb = 9.92 and 9.94 ppm, respectively; Table 1) were derived from a heterogeneous magmatic source.

Table 3. Sr and Nd isotope data for principal rock lithologies in the Poperechny Fe-Mn deposit.

Sample#	3-10	4-08	4-17	128-1	789	789-д	117
Rock Type	Eb1	Eb2	Eb3	FMo	Do1	Do2	Dl
Rb (ppm)	0.88	178.2	1.18	149.6	2.71	9.1	0.6
Sr (ppm)	3.59	88	4.29	163	9.28	200	71
⁸⁷ Rb/ ⁸⁶ Sr	0.7124	5.8887	0.7925	2.6633	0.8450	0.1325	0.0240
⁸⁷ Sr/ ⁸⁶ Sr	0.713988	0.752422	0.715581	0.724809	0.709951	0.705883	0.707933
±2 SD	5	4	8	5	5	4	5
(⁸⁷ Sr/ ⁸⁶ Sr) _i	0.71277	0.74238	0.71423	0.72027	0.70851	0.70566	0.70789
Sm (ppm)	1.62	2.66	2.07	0.58	2.28	2.76	1.04
Nd (ppm)	11.59	19.09	12.08	2.19	7.48	8.75	5.15
¹⁴⁷ Sm/ ¹⁴⁴ Nd	0.0846	0.0841	0.1038	0.1599	0.1842	0.1905	0.1224
¹⁴³ Nd/ ¹⁴⁴ Nd	0.512017	0.511975	0.512109	0.512408	0.512728	0.512737	0.512127
±2 SD	3	4	4	10	5	8	4
ε _{Nd} (t)	−10.40	−11.21	−8.90	−3.92	1.95	2.03	−8.83

Note: Eb—explosive breccia, FMo—Fe-Mn ore, Do—dolerite dikes, Dl—dolomite.

5. Discussion

Iron–manganese mineralization in the Lesser Khingan Range (LKR) of the Russian Far East (Kostenga, Kaylan and Poperechny deposits) is hosted in Vendian–Cambrian carbonates and closely associated with a variety of explosive volcanic rocks. The latter include intermediate to felsic volcanic breccia, variably mineralized lithocrystalloclastic tuffs and magnetite-rich lavas [68–75]. Iron and iron–manganese mineralization is represented by massive and finely laminated ore (Figures 2a–d and 3a,c–f) composed of magnetite, hematite, braunite, haussmanite, rhodochrosite and pyrolusite with minor quartz, chlorite, sericite, gedritic–gruneritic amphibole, monazite and apatite [68,72,75]. Both Fe- and Fe–Mn mineralization and host Neoproterozoic carbonates are intruded by explosive andesitic to rhyolitic breccia (discordant contacts in Figure 3b,c), indicating its magmatic origin and post-Precambrian emplacement. Locally, finely laminated ore is interbedded with explosive volcanic breccia and mineralized tuff (Figure 3a,c–e) or contains numerous thin tephra-rich horizons (Figure 3f). Many samples of explosive volcanic rocks are intensely ferruginized and partially replaced with hydrothermal Fe–Mn mineralization. These observations suggest that at least some part of the Fe–Mn ore formation is contemporaneous with and/or post-dates the intermediate to felsic explosive volcanism. The presence of magnetite-rich lava (Figures 4e,f and 6a–c; Table 2) that is compositionally similar to the El Laco magnetite flows in northern Chile [110] at Kostenga and Poperechny sites further attests to the importance of Fe-rich melts in the formation of the LKR iron- and iron–manganese deposits [68–75]. The entire carbonate-hosted, volcanic–hydrothermal package is later overprinted with low-temperature metasomatic alterations including albite, chlorite, sericite and quartz.

Earlier publications proposed the Late Precambrian (Late Riphean–Vendian) age and volcanogenic–sedimentary origin of the Fe–Mn mineralization in the LKR, primarily on the basis of their concordant geologic relationships with host dolomite and limestone of the Neoproterozoic Murandavsky suite [63–66]. Modern U–Pb age determinations of detrital zircons yielded younger ages of 535 ± 6 Ma, linking the formation of Murandavsky carbonates to the Neoproterozoic–Lower Cambrian boundary [111]. Recently, based on the geology, mineralogy and geochemistry of Fe–Mn mineralization and its close spatial and temporal association with explosive volcanism (“fluidolites”), Berdnikov and co-authors primarily suggested hydrothermal Fe- and Fe–Mn ore formation in the LKR on the basis of geochemical information [68]. For example, LKR ores plot into the field of hydrothermal Fe–Mn formations in $(\text{Ce}/\text{Ce}^*)_{\text{N}} - (\text{Y}/\text{Ho})_{\text{N}}$, Si-Al , $\text{Fe-Mn}-(\text{Co} + \text{Ni} + \text{Cu}) \times 10$ and $(\text{Co} + \text{Ni}) - (\text{Zn} + \text{Cu} + \text{V} + \text{Pb})$ discrimination diagrams for Fe–Mn mineralization [68]. Various geochemical indicator ratios in most iron–manganese ores from the LKR such as $(\text{Mn} + \text{Fe})/\text{Ti}$ (109–193), Ba/Ti (>0.15), Y/Ho (21–35), $(\text{Y}/\text{Y}^*)_{\text{N}}$ (>1), $(\text{Eu}/\text{Eu}^*)_{\text{N}}$ (>1), along with relatively low total REE + Y (<100 ppm) and Th (0.46–7.93 ppm), are compatible with the hydrothermal origin of iron and manganese minerals in the LKR. In particular, the positive Eu anomaly and the lack of a negative Ce anomaly in the majority of ore samples from the LKR deposits argue against any substantial role of seawater precipitation in the formation of Fe–Mn oxides and hydroxides [112–116]. However, in individual samples from the Poperechny deposit, some of these indicator parameters are compatible with the hydrogenic Fe–Mn mineral formation [117–119] suggesting that, at least locally in the LKR, a limited hydrogenic (seawater) component was also involved in the ore formation process [68].

Age constraints on the hydrothermal Fe–Mn ore formation and explosive volcanism in the LKR are quite limited and primarily based on the documented intrusive relationships between intermediate to felsic breccia, Vendian–Cambrian carbonates and iron–manganese ores (Figure 3b,c), along with the new model Sm–Nd ages reported in this study (Table 3). Model Sm–Nd ages of from 1338 to 1864 Ma suggest the presence of a Proterozoic crustal component. In addition, voluminous rhyolite volcanism in the LKR, which is texturally and compositionally similar to the dacitic–rhyolitic tuffs and explosive breccia associated with Poperechny, Kostenga and Kaylan Fe–Mn deposits, was dated by SHRIMP-II at

102.98 ± 0.57 Ma and 103.58 ± 0.35 Ma [120]. Interestingly, Cretaceous magmatism (granite and diorite porphyry, andesites, dacites, rhyolites) within the Chinese portion of the Lesser Khingan Range is dated at 107–124 Ma, and is associated with the prolific Au mineralization throughout the Chinese LKR [121–123]. It is important to emphasize that all Fe-Mn deposits within the Russian part of the LKR contain substantial amounts of native Au, gold-bearing alloys and other precious metal minerals (Figures 5c and 6d–f), and are locally associated with economic precious metal grades in excess of 13 g/t of combined Au + PGE [68–75]. It has been proposed that Cretaceous magmatism and associated ore-forming processes (Fe-Mn, Au-Ag-PGE, etc.) in the LKR are potentially linked to the complex tectonic processes related to the subduction of the Paleo-Pacific (Izanagi) plate under the edge of the Eurasian continent [62,85,124–128].

The geochemical characteristics of Fe-Mn mineralization and associated igneous rocks suggest a broad subduction-related origin. Pyroclastic rocks and magnetite-rich lavas from the LKR iron–manganese deposits form strongly differentiated (picrite to rhyolite; Figure 7a) volcanic suites primarily belonging to low-K and high-K types (Figure 7b), not unlike the differentiated low-K tholeiitic, calc-alkaline and shoshonitic magma types typical of the Circum-Pacific convergent margins [129–136]. Trace element distribution, specifically the relatively high LILE/HFSE, LILE/LREE and LILE/HREE ratios coupled with distinctive negative HFSE (Nb, Ta, Hf and Zr; Figure 8) anomalies in volcanic explosive rocks and magnetite-rich lavas, suggest their derivation from subduction-related sources. Their presence among volcanic breccia samples with high MgO contents (8–11 wt.%; [68,72–75]) is supportive of the differentiation of mantle-derived magma as a primary petrogenetic process [72–75]. This is also consistent with the unusually high Ni contents (276–558 ppm) in some basaltic andesites and andesites from the Poperechny deposit indicative of primary, mantle-derived mafic and intermediate melts for the LKR volcanics [72]. It is also possible that some dacitic to rhyolitic volcanic rocks with very low MgO, Cr and Ni contents and high Ba/Nb, Ba/La, Rb/Y and La/Ta ratios could be direct melting products of the mafic lower crust beneath the NE Asian convergent margin [72,78]. The iron–manganese ore in the LKR is also characterized by prominent HFSE depletions (especially, Ta) in primitive mantle-normalized patterns and, with the exception of the Kaylan deposit, general enrichment in LILE with respect to the rare earth elements (Figure 8c,f,i). Uranium enrichments in the Fe-Mn mineralization at the Kostenga and Poperechny deposits (Figure 8c,f) are also indicative of their predominantly hydrothermal origin due to the uptake of uranium by phosphates (monazite, xenotime) and Fe-Mn oxides (for example, hematite) under hydrothermal conditions [137–140]. Monazite, xenotime, and hematite are common mineral phases in the LKR iron–manganese ores (Figure 5a,b,d,e). Dolerite intrusions associated with the LKR mineralization display elevated HFSE concentrations (~9 ppm Nb; Table 2), which are comparable to the high-Nb basalt (HNB) magmas in subduction zones [141,142]. The HNB melts in modern and ancient magmatic arcs are believed to be products of adakite–mantle wedge interactions and, in case of the LKR dolerites, may indicate the possible involvement of the downgoing or stagnant Paleo-Pacific slab beneath the NE Asian convergent margin in the Mesozoic magmatism within the LKR.

Strontium and neodymium isotopes provide some further insights into the formation of Fe-Mn deposits in the LKR. Explosive volcanic breccia exhibits highly radiogenic $^{87}\text{Sr}/^{86}\text{Sr}$ isotope ratios (up to 0.752422) and low radiogenic Nd isotope composition ($\epsilon_{\text{Nd}}(t)$ of from -8.90 to -11.21), can be plotted in the field of marine sediments [143] and is close to the characteristic values of Phanerozoic granites within the Central Asian Orogenic Belt [144,145] and ancient upper continental crust on the $\epsilon_{\text{Nd}}(t) - ^{87}\text{Sr}/^{86}\text{Sr}$ diagram (Figure 10).

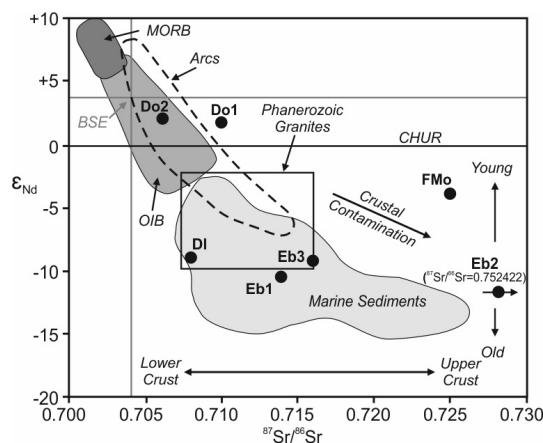


Figure 10. Variations of Sr and Nd isotopes in principal rock types from the LKR Fe-Mn deposits. Fields for mid-ocean ridge basalts (MORB), ocean island basalts (OIB), arc volcanics (Arcs) and estimated values for the Bulk Silicate Earth (BSE) are from [109]. Field for Phanerozoic granites is from [144]. Field of marine sediments is based on [143]. Ranges for lower and upper crust and old versus young continental crust are based on [108,109]. Sample identifications: explosive breccia Eb1 = 3-10, Eb2 = 4-08, Eb3 = 4-17; ore FMO = 128-1, dolerite Do1 = 789, Do2 = 789-Д, host dolomite DI = 117 (see Table 1 for major and trace element compositions of these samples).

Host dolomite shares a radiogenic Nd-isotopic signature ($\epsilon_{Nd}(t)$ of -8.83 ; Table 3) with the LKR explosive breccia but displays a less radiogenic Sr-isotope composition. The host dolomite is still plotted in the marine sediment field of [109] (Figure 10). The iron–manganese ore has a less radiogenic isotopic composition of neodymium and highly radiogenic Sr-isotope ratios, suggesting the involvement of a juvenile crust in their formation at the NE Asian convergent margin. However, both volcanic explosive breccia and associated Fe-Mn mineralization experienced protracted contamination with both ancient and juvenile crustal components. Nd-isotope variations suggest that the Nd signature may have been introduced by the assimilation of Neoproterozoic carbonates, as volcanic breccia contains abundant dolomite clasts and xenoliths (Figures 2–4). However, the extremely radiogenic Sr-isotope compositions of some explosive breccia indicate the involvement of an ancient upper continental crust, probably not unlike some Precambrian clastic sediments. Such clastic metasediments are known within the Jiamusi terrane in NE China and their isotopic characteristics may be a suitable contaminant component for the Mesozoic volcanism throughout the eastern part of the CAOB [146]. Both ancient and juvenile crust were involved in the formation and evolution of the CAOB, as indicated by abundant geologic, geochronological and isotopic data [147–152], and both upper crustal types, based on the Nd-Sr signature (Figure 10), may have participated in the formation of volcanic rocks and the Fe-Mn mineralization in the LKR. Later-stage dolerite intrusions display less radiogenic Nd-Sr isotope characteristics (Figure 10) and are broadly similar to arc-related volcanic rocks, possibly representing the radiogenic isotope signature of the mantle beneath the LKR and easternmost segment of the CAOB.

Carbon isotopes are currently successfully used to trace deep carbon recycling and processing through various parts of the subduction and collision zones [153–157]. $\delta^{13}C$ variations in explosive volcanic breccia (from -24.5 to -28.4 ‰), iron–manganese ore (from -25.2 to -29.4 ‰) and host Vendian–Cambrian carbonates (from -22.0 to -28.3 ‰) are similar to the isotopic $\delta^{13}C$ signature of biogenic carbon, which average -25 ‰ over more than 3.8 Ga of the Earth’s planetary evolution [158–160]. These values are comparable to the very light carbon isotope signature of some asthenospheric and lithospheric diamonds ($\delta^{13}C$ from -10 ‰ to -40 ‰; [155,161,162]) and moissanites ($\delta^{13}C$ from -18 ‰ to -35 ‰; [163–165]) brought to the surface in kimberlite and lamproite-like magmas, and tectonically exhumed high-pressure chromitites that appear to record the deep subduction zone recycling of biogenic carbon into the planetary mantle [154]. Pore fluids generated

from the accretionary prism of the Cascadia active continental margin have a $\delta^{13}\text{C}$ of -35% to -63% [166], while carbon isotope composition in calcite veins from the Shimanto accretionary complex in southwest Japan is estimated to range from -10% to -19% [167]. The carbon isotope composition of volcanic gases emitted from arc volcanoes along the Andean, Aleutian–Alaskan and Costa Rican convergent margins is more variable and somewhat heavier, at a $\delta^{13}\text{C}$ ranging from $+3\%$ to -21% , which may reflect the small-scale mixing of carbon sources and fluid–fluid/fluid–solid interactions that occur during outgassing within these subduction zone environments [168–170]. Hydrothermal fluids at convergent margins are characterized by predominantly negative and highly variable C-isotope values, which are commonly interpreted as the result of the subduction zone recycling of both biogenic matter and abiogenic (carbonates) sediments, followed by carbon outgassing through arc volcanoes, accretionary prisms and submarine hydrothermal vents [154,171–173]. At least in one case of the submarine Brothers volcano in the Kermadec arc, $\delta^{13}\text{C}$ -depleted hydrothermal fluids are associated with elevated Fe and Mn fluxes in the typical subduction zone tectonic setting [174]. Berdnikov and his co-authors have previously interpreted a highly negative carbon isotope signature in the iron–manganese ore and explosive breccia from the LKR to be the result of biogenic carbon recycling through the paleo-subduction zone at the edge of the Asian continental mass [68].

The formation of such unusual iron and iron–manganese hydrothermal mineralization in association with explosive Fe-rich magmatism (Fe-rich lavas and tuffs) is still insufficiently studied and poorly understood [25,32,35–38,41,110]. However, further research into deposits of this type appears to be quite important, as a better understanding of magmatic–hydrothermal iron deposits may provide a solid foundation for adequate genetic models and guide successful exploration activities in various prospective regions worldwide. One of the possible models of the formation of Fe–Mn mineralization in the Lesser Khingan Region is presented in Figure 11.

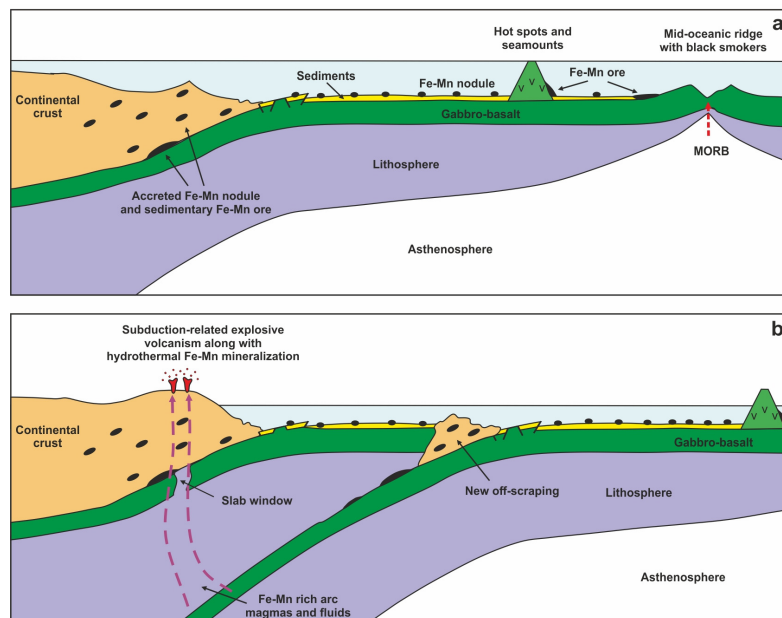


Figure 11. Plate tectonic model for the formation of LKR Fe–Mn mineralization along the Pacific-type convergent plate boundary (modified after [18]). Figures a and b depict different temporal stages in the formation of the LKR Fe–Mn mineralization: (a) Late Jurassic–Early Cretaceous, and (b) end of the Early Cretaceous [175,176].

We propose that LKR Fe- and Fe–Mn mineralization was formed as a result of the complex interplay between the processes of marine sedimentation coupled with multi-stage subduction (Figure 11). Earlier, Golozubov and Khanchuk [175] suggested that during the Late Jurassic–Early Cretaceous period, the fossil Izanagi plate experienced

protracted flat subduction beneath the Jiamusi–Bureya–Khanka super-terrane (Figure 11a). This flat subduction was accompanied by the formation of compressional structures and off-scraping frontal accretion, involving rocks enriched in sedimentary manganese and iron [18,54,70]. At the end of the Early Cretaceous, the deep-sea trench shifted to the east [176]. Devolatilization and partial melting of the new slab generated an upwelling flow composed of Fe-rich melts and fluids, which scavenged additional ore components during their ascent through the previously formed mineralized accretionary complexes. It is also possible that the generation of these metal-rich magmas and fluids and their emplacement in the shallow crust was further facilitated by the formation of slab window environments in the flattened oceanic slab [175]. The contamination of upwelling ore-forming magmas and fluids by the underlying ancient continental crust resulted in the strongly radiogenic Nd isotope signature observed in volcanic rocks associated with Fe–Mn mineralization in the Lesser Khingan Range of the Russian Far East.

6. Conclusions

1. Iron and iron–manganese deposits and showings form several closely spaced clusters in the Lesser Khingan Range of the Russian Far East. Mineralization is composed of magnetite, hematite, braunite, hausmannite, rhodochrosite and pyrolusite, hosted in Vendian–Cambrian carbonates. Fe- and Fe–Mn ores are intruded by explosive breccia, tuffaceous pyroclastic formations and “magnetite lava”, and are occasionally interbedded with the latter. Locally, hydrothermal Fe–Mn mineralization is developed over igneous material.
2. The geochemical characteristics of volcanic rocks and Fe- and Fe–Mn mineralization in the LKR suggest that they were produced from subduction-related mantle and crustal sources, most probably within the active continental margin of NE Asia.
3. Textural, mineralogical, and geochemical features of the Fe- and Fe–Mn ores support their formation under hydrothermal conditions (possibly with some minor input from hydrogenic processes) in association with active explosive basaltic to rhyolitic volcanism and prolific submarine hydrothermal vents. Carbon isotopes also suggest the involvement of the recycled pelagic component in the formation of iron–manganese ores and associated volcanic rocks.
4. Sr and Nd isotope variations in products of explosive volcanism and Fe–Mn ore indicate the pervasive contamination of the ore-forming volcanic–hydrothermal system with ancient and juvenile continental crusts. Later-stage dolerite magmas represent primary mafic melts derived from the subduction-modified mantle domains beneath the northeastern edge of the Asian continental mass.

Author Contributions: Conceptualization, N.B. and P.K.; methodology, N.B., P.K. and V.N.; software, N.B.; validation, N.B., P.K. and V.N.; formal analysis, N.B., P.K., V.N., V.K., N.K. and V.S.; investigation, N.B., P.K., V.N., V.K., N.K. and V.S.; data curation, N.B.; writing—original draft preparation, N.B. and P.K.; writing—review and editing, N.B., P.K., V.N. and V.S.; visualization, N.B.; supervision, N.B. and P.K.; project administration, N.B.; funding acquisition, N.B. All authors have read and agreed to the published version of the manuscript.

Funding: The study was performed in the context of the Government Assignments to the Institute of Tectonics and Geophysics, Far East Branch, Russian Academy of Sciences, Institute of Precambrian Geology and Geochronology of the Russian Academy of Sciences with financial support from the Russian Science Foundation, grant 22-17-00023 and Institute for Precambrian Geology and Geochronology (IPGG) grant number FMUW-2022-0005.

Data Availability Statement: Data are available upon request from the correspondent author.

Acknowledgments: This paper benefited from the constructive reviews by two anonymous reviewers. We thank our colleagues from the Far East Fund for Geological Data (Khabarovsk, Russian Federation) for providing us with representative collection of samples of magnetite–hematite ores and pyroclastic rocks from the Kostenga and Kaylan deposits.

Conflicts of Interest: The authors declare no conflict of interest.

References

1. Park, C.F., Jr. The spilitite and manganese problems of the Olympic Peninsula, Washington. *Am. J. Sci.* **1946**, *244*, 305–323. [[CrossRef](#)]
2. Simons, F.S.; Straczek, J.A. *Geology of Manganese Deposits of Cuba*; U.S. Government Publishing Office: Washington, DC, USA, 1958; Volume 1057, pp. 1–289.
3. Maksimov, A.A. Types of manganese and iron-manganese deposits in Central Kazakhstan. *Int. Geol. Rev.* **1960**, *2*, 508–521. [[CrossRef](#)]
4. Reed, J.J. Manganese ore in New Zealand. *N. Z. J. Geol. Geophys.* **1960**, *3*, 344–354.
5. Elderfield, H.; Gass, I.G.; Hammond, A.; Bear, L.M. The origin of ferromanganese sediments associated with the Troodos Massif of Cyprus. *Sedimentology* **1972**, *19*, 1–19. [[CrossRef](#)]
6. Thonis, M.; Burns, R.G. Manganese ore deposits and plate tectonics. *Nature* **1975**, *253*, 614–616. [[CrossRef](#)]
7. Bonatti, E.; Zerbi, M.; Kay, R.; Rydell, H.S. Metalliferous deposits from the Apennine ophiolites: Mesozoic equivalents of modern deposits from oceanic spreading centre. *Geol. Soc. Am. Bull.* **1976**, *87*, 83–94. [[CrossRef](#)]
8. Snyder, W.S. Manganese deposited by submarine hot springs in chert-greenstone complexes, western United States. *Geology* **1978**, *6*, 741–744. [[CrossRef](#)]
9. Sokolova, E.A. *Manganese-Bearing Volcanogeno-Sedimentary Formations*; Nauka Publishers: Moscow, Russia, 1982; pp. 1–196. (In Russian)
10. Glasby, G.P. Hydrothermal manganese deposits in island arcs and related to subduction processes: A possible model for genesis. *Ore Geol. Rev.* **1988**, *4*, 145–153. [[CrossRef](#)]
11. Mosier, D.L.; Page, N.J. *Descriptive and Grade-Tonnage Models of Volcanogenic Manganese Deposits in Oceanic Environments: A Modification*; US Government Printing Office: Washington, DC, USA, 1988; Volume 1811, pp. 1–28.
12. Roy, S. Genetic diversity of manganese deposition in the terrestrial geological record. *Geol. Soc. Spec. Publ.* **1997**, *119*, 5–27. [[CrossRef](#)]
13. Oztürk, H. Manganese deposits in Turkey: Distribution, types and tectonic setting. *Ore Geol. Rev.* **1997**, *12*, 187–203. [[CrossRef](#)]
14. Sillitoe, R.H. Iron oxide-copper-gold deposits: An Andean view. *Mineral. Depos.* **2003**, *38*, 787–812. [[CrossRef](#)]
15. Williams, P.J.; Barton, M.D.; Johnson, D.A.; Fontboté, L.; de Haller, A.; Mark, G.; Oliver, N.H.S.; Marschik, R. Iron oxide copper-gold deposits: Space-time distribution, and possible modes of origin. *Econ. Geol.* **2005**, *100*, 371–405.
16. Chen, H.; Clark, A.H.; Kyser, T.K.; Ullrich, T.D.; Baxter, R.; Chen, Y.; Moody, T. Evolution of the giant Marcona-Mina Justa iron oxide-copper-gold district, south-central Peru. *Econ. Geol.* **2010**, *105*, 155–185. [[CrossRef](#)]
17. Groves, D.I.; Bierlein, F.P.; Meinert, L.D.; Hitzman, M.W. Iron oxide copper-gold (IOCG) deposits through Earth history: Implications for origin, lithospheric setting, and distinction from other epigenetic iron oxide deposits. *Econ. Geol.* **2010**, *105*, 641–654. [[CrossRef](#)]
18. Nakagawa, M.; Santosh, M.; Maruyama, S. Manganese formations in the accretionary belts of Japan: Implications for subduction-accretion process in an active convergent margin. *J. Asian Earth Sci.* **2011**, *42*, 208–222. [[CrossRef](#)]
19. Chen, H.; Cooke, D.R.; Baker, M.J. Mesozoic iron oxide copper-gold mineralization in the Central Andes and the Gondwana supercontinent breakup. *Econ. Geol.* **2013**, *108*, 37–44. [[CrossRef](#)]
20. Jonsson, E.; Troll, V.R.; Hoegdahl, K.; Harris, C.; Weis, F.; Nilsson, K.P.; Skelton, A. Magmatic origin of giant “Kiruna-type” apatite-iron oxide ores in Central Sweden. *Sci. Rep.* **2013**, *3*, 1644–1652. [[CrossRef](#)] [[PubMed](#)]
21. Chai, F.; Yang, F.; Liu, F.; Santosh, M.; Geng, X.; Li, Q.; Liu, G. The Abagong apatite-rich magnetite deposit in the Chinese Altay Orogenic Belt: A Kiruna-type iron deposit. *Ore Geol. Rev.* **2014**, *57*, 482–497. [[CrossRef](#)]
22. Zhang, Z.; Hong, W.; Jiang, Z.; Duan, S.; Li, F.; Shi, F. Geological characteristics and metallogenesis of iron deposits in western Tianshan, China. *Ore Geol. Rev.* **2014**, *57*, 425–440. [[CrossRef](#)]
23. Günther, T.; Klemd, R.; Zhang, X.; Horn, I.; Weyer, S. In-situ trace element and Fe-isotope studies on magnetite of the volcanic-hosted Zhibo and Chagangnuoer iron ore deposits in the Western Tianshan, NW China. *Chem. Geol.* **2017**, *453*, 111–127. [[CrossRef](#)]
24. Maghfouri, S.; Rastad, E.; Mousivand, F.; Choulet, F.; Ye, L. Geological and geochemical constraints on the Cheshmeh-Frezi volcanogenic stratiform manganese deposit, southwest Sabzevar basin, Iran. *Ore Geol. Rev.* **2017**, *89*, 96–113. [[CrossRef](#)]
25. Simon, A.C.; Knipping, J.; Reich, M.; Barra, F.; Deditius, A.P.; Bilenker, L.; Childress, T. Kiruna-type iron oxide-apatite (IOA) and iron oxide copper-gold (IOCG) deposits form by a combination of igneous and magmatic-hydrothermal processes: Evidence from the Chilean Iron Belt. *SEG Spec. Publ.* **2018**, *21*, 89–114.
26. Liang, P.; Chen, H.; Han, J.; Wu, C.; Zhang, W.; Xu, D.; Lai, C.-K.; Kyser, K. Iron oxide-copper-gold mineralization of the Devonian Laoshankou deposit (Xinjiang, NW China) in the Central Asian Orogenic Belt. *Ore Geol. Rev.* **2019**, *104*, 628–655. [[CrossRef](#)]
27. Xu, H.; Gao, J.; Yang, R.; Feng, K.; Wang, L.; Chen, J. Metallogenic mechanism of large manganese deposits from Permian manganese ore belt in western South China Block: New mineralogical and geochemical evidence. *Ore Geol. Rev.* **2021**, *132*, 103993. [[CrossRef](#)]
28. Skirrow, R.G. Iron oxide copper-gold (IOCG) deposits—A review (part 1): Settings, mineralogy, ore geochemistry and classification. *Ore Geol. Rev.* **2022**, *140*, 104569. [[CrossRef](#)]

29. Zhang, B.-L.; Lv, Z.-C.; Dong, Z.-G.; Zhang, X.; Yu, X.-F.; Li, Y.-S.; Zhen, S.-M.; Wang, C.-L. Source characteristics of the Carboniferous Ortokarnash manganese deposit in the Western Kunlun Mountains. *Minerals* **2022**, *12*, 786. [[CrossRef](#)]
30. Li, H.; Zhang, Z.; Liu, B.; Jin, Y.; Santosh, M. The genetic link between iron oxide-apatite and iron skarn mineralization in the Beizhan deposit, Western Tianshan, NW China: Evidence from magnetite and gangue mineral geochemistry. *J. Asian Earth Sci.* **2023**, *241*, 105460. [[CrossRef](#)]
31. Frutos, J.; Oyarzun, J.M. Tectonic and geochemical evidence concerning the genesis of El Laco magnetite lava flow deposits, Chile. *Econ. Geol.* **1975**, *70*, 988–990. [[CrossRef](#)]
32. Nyström, J.O.; Henríquez, F. Magmatic features of iron ores of the Kiruna type in Chile and Sweden: Ore textures and magnetite geochemistry. *Econ. Geol.* **1994**, *89*, 820–830. [[CrossRef](#)]
33. Barton, M.D.; Johnson, D.A. Evaporitic-source model for igneous-related Fe oxide-(REE-Cu-Au-U) mineralization. *Geology* **1996**, *24*, 259–262. [[CrossRef](#)]
34. Sillitoe, R.H.; Burrows, D.R. New field evidence bearing on the origin of the El Laco magnetite deposit, Northern Chile. *Econ. Geol.* **2002**, *97*, 1101–1109.
35. Dare, S.A.S.; Barnes, S.-J.; Beaudoin, G. Did the massive magnetite “lava flows” of El Laco (Chile) form by magmatic or hydrothermal processes? New constraints from magnetite composition by LA-ICP-MS. *Mineral. Depos.* **2015**, *50*, 607–617. [[CrossRef](#)]
36. Velasco, F.; Tornos, F.; Hanchar, J.M. Immiscible iron- and silica-rich melts and magnetite geochemistry at the El Laco volcano (northern Chile): Evidence for a magmatic origin for the magnetite deposits. *Ore Geol. Rev.* **2016**, *79*, 346–366. [[CrossRef](#)]
37. Tornos, F.; Velasco, F.; Hanchar, J.M. The magmatic to magmatic-hydrothermal evolution of the El Laco deposit (Chile) and its implications for the genesis of magnetite-apatite deposits. *Econ. Geol.* **2017**, *112*, 1595–1628. [[CrossRef](#)]
38. Ovalle, J.T.; La Cruz, N.L.; Reich, M.; Barra, F.; Simon, A.C.; Konecke, B.A.; Rodriguez-Mustafa, M.A.; Deditius, A.P.; Childress, T.M.; Morata, D. Formation of massive iron deposits linked to explosive volcanic eruptions. *Sci. Rep.* **2018**, *8*, 14855. [[CrossRef](#)] [[PubMed](#)]
39. Yu, W.; Polgári, M.; Fintor, K.; Gyollai, I.; Szabó, M.; Velledits, F.; Liu, Z.; Du, Y. Contribution of microbial processes to the enrichment of Middle Permian manganese deposits in northern Guizhou, South China. *Ore Geol. Rev.* **2021**, *136*, 104259. [[CrossRef](#)]
40. Polgári, M.; Gyollai, I. Comparative study of formation conditions of Fe-Mn ore microbialities based on mineral assemblages: A critical self-overview. *Minerals* **2022**, *12*, 1273. [[CrossRef](#)]
41. Tornos, F.; Hanchar, J.M.; Munizaga, R.; Velasco, F.; Galindo, C. The role of the subducting slab and melt crystallization in the formation of magnetite-(apatite) systems, Coastal Cordillera of Chile. *Mineral. Deposita* **2021**, *56*, 253–278. [[CrossRef](#)]
42. Longman, J.; Palmer, M.R.; Gernon, T.M.; Manners, H.R.; Jones, M.T. Subaerial volcanism is a potentially major contributor to oceanic iron and manganese cycles. *Commun. Earth Environ.* **2022**, *3*, 60. [[CrossRef](#)]
43. Keller, T.; Tornos, F.; Hanchar, J.M.; Pietruszka, D.K.; Soldati, A.; Dingwell, D.B.; Suckale, J. Genetic model of the El Laco magnetite-apatite deposits by extrusion of iron-rich melt. *Nat. Commun.* **2022**, *13*, 6114. [[CrossRef](#)]
44. Eugster, H.P.; Chou, I.M. A model for the deposition of Cornwall-type magnetite deposits. *Econ. Geol.* **1979**, *74*, 763–774. [[CrossRef](#)]
45. Rose, A.W.; Herrick, D.C.; Deines, P. An oxygen and sulfur isotope study of skarn-type magnetite deposits of the Cornwall type, southeastern Pennsylvania. *Econ. Geol.* **1985**, *80*, 418–443. [[CrossRef](#)]
46. Xie, Q.; Zhan, Z.; Hou, T.; Jin, Z.; Santosh, M. Geochemistry and oxygen isotope composition of magnetite from the Zhangmatun deposit, North China Craton: Implications for the magmatic-hydrothermal evolution of Cornwall-type iron mineralization. *Ore Geol. Rev.* **2017**, *88*, 57–70. [[CrossRef](#)]
47. Cronan, D.S.; Glasby, G.P.; Moorby, S.A.; Thomson, J.; Knedler, K.E.; McDougall, J.C. A submarine hydrothermal manganese deposit from the south-west Pacific Island arc. *Nature* **1982**, *298*, 456–458. [[CrossRef](#)]
48. Usui, A.; Nishimura, A. Submersible observations of hydrothermal manganese deposits on the Kaikata Seamount, Izu-Ogasawara (Bonin) Arc. *Mar. Geol.* **1992**, *106*, 203–216. [[CrossRef](#)]
49. Savelli, C.; Marani, M.; Gamberi, F. Geochemistry of metalliferous, hydrothermal deposits in the Aeolian arc (Tyrrhenian Sea). *J. Volcanol. Geotherm. Res.* **1999**, *88*, 302–323. [[CrossRef](#)]
50. Hein, J.R.; Stamatakis, M.G.; Dowking, J.S. Trace metal-rich Quaternary hydrothermal manganese oxide and barite, Milos Island, Greece. *Appl. Earth Sci.* **2000**, *109*, 67–76. [[CrossRef](#)]
51. Rogers, T.D.S.; Hodgkinson, R.A.; Cronan, D.S. Hydrothermal manganese deposits from the Tonga-Kermadec Ridge and Lau Basin region, southwest Pacific. *Mar. Georesources Geotechnol.* **2001**, *19*, 245–268.
52. Liakopoulos, A.; Glasby, G.P.; Papavassiliou, C.T.; Boulegue, J. Nature and origin of the Vani manganese deposit, Milos, Greece: An overview. *Ore Geol. Rev.* **2001**, *18*, 181–2009. [[CrossRef](#)]
53. Glasby, G.P.; Cherkashov, G.A.; Gavrilenko, G.M.; Rashidov, V.A.; Slotvsov, I.B. Submarine hydrothermal activity and mineralization on the Kurile and western Aleutian Island arcs, N.W. Pacific. *Mar. Geol.* **2006**, *231*, 163–180. [[CrossRef](#)]
54. Hein, J.R.; Schulz, M.S.; Dunham, R.E.; Stern, R.J.; Bloomer, S.H. Diffuse flow hydrothermal manganese mineralization along the active Mariana and southern Izu-Bonin arc system, western Pacific. *J. Geophys. Res.* **2008**, *113*, 1–29. [[CrossRef](#)]
55. Dubinin, A.V.; Uspenskaya, T.Y.; Gavrilenko, G.M.; Rashidov, V.A. Geochemistry and genesis of Fe-Mn mineralization in island arcs in the west Pacific Ocean. *Geochem. Int.* **2008**, *46*, 1206–1227. [[CrossRef](#)]

56. Baturin, G.N. Geochemistry of hydrothermal ferromanganese crusts of the Sea of Japan. *Dokl. Earth Sci.* **2012**, *445*, 862–867. [[CrossRef](#)]
57. Baturin, G.N.; Dubinchuk, V.T.; Rashidov, V.A. Ferromanganese crusts from the Sea of Okhotsk. *Oceanology* **2012**, *52*, 88–100. [[CrossRef](#)]
58. Pelleter, E.; Fouquet, Y.; Etoubleau, J.; Cheron, S.; Labanieh, S.; Josso, P.; Bollinger, C.; Langlade, J. Ni-Cu-Co-rich hydrothermal manganese mineralization in the Wallis and Futuna back-arc environment (SW Pacific). *Ore Geol. Rev.* **2017**, *87*, 126–146. [[CrossRef](#)]
59. Knaack, D.R.; Sullivan, K.; Brown, D.J.; Langa, M.; Mathieu, J.; Bouchard, M.L.; Haring, M.; Petrus, J.; Stern, R.J.; Hein, J.R.; et al. Geochemical and mineralogical composition of ferromanganese precipitates from the southern Mariana arc: Evaluation, formation, and implications. *Chem. Geol.* **2021**, *568*, 120132. [[CrossRef](#)]
60. Parfenov, L.M.; Berzin, N.A.; Khanchuk, A.I.; Badarch, G.; Belichenko, V.G.; Bulgatov, A.N.; Dril, S.I.; Kirillova, G.L.; Kuzmin, M.I.; Nokleberg, W.D.; et al. Model of formation of orogenic belts of the central and northeastern Asia. *Tikhookean Geol.* **2003**, *22*, 7–41.
61. Wilde, S.A.; Wu, F.-Y.; Zhao, G. The Khanka Block, NE China, and its significance for the evolution of the Central Asian Orogenic Belt and continental accretion. *Geol. Soc. Lond. Spec. Publ.* **2010**, *338*, 117–137. [[CrossRef](#)]
62. Khanchuk, A.I.; Alenicheva, A.A.; Golozubov, V.V.; Kandaurov, A.T.; Yurchenko, Y.Y.; Sergeev, S.A. The Khanka Massif: The heterogeneity of its basement and regional correlations. *Russ. J. Pac. Geol.* **2022**, *16*, 281–299. [[CrossRef](#)]
63. Egorov, E.V.; Timofeieva, M.W. Effusive Iron-Silica Formations and Iron-Ore Deposits of the Maly Khingan. In *Genesis of Iron and Manganese Deposits, Proceedings of Kiev Symposium*; UNESCO: Paris, France, 1973; pp. 181–185.
64. Chebotarev, M.V. Geological structures of the South Khingan manganese deposit and essential composition of its ores. *Int. Geol. Rev.* **1960**, *2*, 851–866. [[CrossRef](#)]
65. Zhirnov, A.M. New Russian iron ore basin in the Jewish Autonomous Region (Far East). *Ores Met.* **2008**, *5*, 16–26. (In Russian)
66. Zhirnov, A.M. Russian new gold-cobalt-uranium-manganese-iron and graphite giants in the Jewish Autonomous Region (Far East). *Discovery* **2015**, *38*, 1–6.
67. Alexandrov, E.A. The Precambrian banded iron-formations of the Soviet Union. *Econ. Geol.* **1973**, *68*, 1035–1062. [[CrossRef](#)]
68. Berdnikov, N.V.; Nevstruev, V.G.; Saksin, B.G. Sources and formation conditions of ferromanganese mineralization of the Bureya and Khanka massifs, Russian Far East. *Russ. J. Pac. Geol.* **2016**, *10*, 263–273. [[CrossRef](#)]
69. Khanchuk, A.I.; Rasskazov, I.Y.; Kryukov, V.G.; Litvinova, N.M.; Saksin, B.G. Finds of economic platinum in ores from the South Khingan Mn deposit. *Dokl. Earth Sci.* **2016**, *470*, 1031–1033. [[CrossRef](#)]
70. Berdnikov, N.V.; Nevstruev, V.G.; Saksin, B.G. Genetic aspects of the noble-metal mineralization at the Poperechnoe deposit, Lesser Khingan, Russia. *Russ. J. Pac. Geol.* **2017**, *11*, 421–435. [[CrossRef](#)]
71. Nevstruev, V.G.; Berdnikov, N.V.; Didenko, A.N.; Saksin, B.G.; Lavrik, N.A. Fluidolites as a source of primary gold-platinum mineralization in the Poperechnoe Deposit (Malyi Khingan Range, Russia). *Dokl. Earth Sci.* **2018**, *482*, 1203–1206. [[CrossRef](#)]
72. Berdnikov, N.V.; Nevstruev, V.G.; Kepezhinskas, P.K.; Mochalov, A.G.; Yakubovich, O.V. PGE mineralization in andesite explosive breccias associated with the Poperechny iron-manganese deposit (Lesser Khingan, Far East Russia); whole-rock geochemical, ^{190}Pt - ^4He isotopic, and mineralogical evidence. *Ore Geol. Rev.* **2020**, *118*, 103352. [[CrossRef](#)]
73. Khanchuk, A.I.; Mochalov, A.G.; Rasskazov, I.Y.; Yakubovich, O.V.; Berdnikov, N.V.; Nevstruyev, V.G. Isotopic age of native platinum from andesitic fluidolites of the Poperechny deposit (Malyi Khingan, Russia). *Russ. J. Pac. Geol.* **2020**, *14*, 43–47. [[CrossRef](#)]
74. Berdnikov, N.V.; Nevstruev, V.G.; Kepezhinskas, P.K.; Krutikova, V.O.; Konovalova, N.S.; Astapov, I.A. Silicate, Fe-oxide, and Au-Cu-Ag microspherules in ores and pyroclastic rocks of the Kostenga iron deposit, in the Far East of Russia. *Russ. J. Pac. Geol.* **2021**, *15*, 236–251. [[CrossRef](#)]
75. Berdnikov, N.; Nevstruev, V.; Kepezhinskas, P.; Astapov, I.; Konovalova, N. Gold in mineralized volcanic systems from the Lesser Khingan Range (Russian Far East): Textural types, composition and possible origins. *Geosciences* **2021**, *11*, 103. [[CrossRef](#)]
76. Smirnov, Y.V.; Sorokin, A.A.; Kudryashov, N.M. Early Paleozoic gabbro-amphibolites in the structure of the Bureya Terrane (eastern part of the Central Asian Fold Belt): First geochronological data and tectonic position. *Dokl. Earth Sci.* **2012**, *445*, 796–801. [[CrossRef](#)]
77. Sal'nikova, E.B.; Kotov, A.B.; Kovach, V.P.; Velikoslavinskii, S.D.; Jahn, B.M.; Sorokin, A.A.; Sorokin, A.P.; Wang, K.-L.; Chan, S.-L.; Li, H.-Y.; et al. Mesozoic age of the Uril formation of the Amur Group, Lesser Khingan terrane of the Central Asian Foldbelt: Results of U-Pb and Lu-Hf isotopic studies of detrital zircons. *Dokl. Earth Sci.* **2013**, *453*, 1181–1184. [[CrossRef](#)]
78. Sorokin, A.A.; Kotov, A.B.; Kudryashov, N.M.; Kovach, V.P. Early Mesozoic granitoid and rhyolite magmatism of the Bureya Terrane of the Central Asian Orogenic Belt: Age and geodynamic settings. *Lithos* **2016**, *261*, 181–194. [[CrossRef](#)]
79. Ovchinnikov, R.O.; Sorokin, A.A.; Kydryashov, N.M. Early Paleozoic magmatic events in the Bureya Continental Massif, Central Asian Orogenic Belt: Timing and tectonic significance. *Lithos* **2021**, *396–397*, 106237. [[CrossRef](#)]
80. Long, X.-Y.; Xu, W.-L.; Yang, H.; Tang, J.; Sorokin, A.A.; Ovchinnikov, R.O. Late Permian-Triassic tectonic nature of the eastern Central Asian Orogenic Belt: Constraints from the geochronology and geochemistry of igneous rocks in the Bureya Massif. *Lithos* **2021**, *380–381*, 105924. [[CrossRef](#)]

81. Yang, H.; Ge, W.; Bi, J.-H.; Wang, Z.-H.; Tian, D.-X.; Dong, Y.; Chen, H.-J. The Neoproterozoic-early Paleozoic evolution of the Jiamusi Block, NE China and its East Gondwana connection: Geochemical and zircon U-Pb-Hf isotopic constraints from the Mashan Complex. *Gondwana Res.* **2018**, *54*, 102–121. [[CrossRef](#)]
82. Yang, H.; Xu, W.-L.; Sorokin, A.A.; Ovchinnikov, R.O.; Wu, H.-R.; Long, X.-Y. Bureya-Jiamusi-Khanka superterrane linked to the Kuunga-Pinjarra interior orogen of East Gondwana and its drift toward Northeast Asia. *Geol. Soc. Am. Bull.* **2023**. [[CrossRef](#)]
83. Smirnova, Y.N.; Sorokin, A.A. Provenance sources of Upper Proterozoic and Lower Paleozoic clastic deposits of the Lesser Khingan terrane, Central Asian Fold belt: U-Pb (LA-ICP-MS) geochronological results. *Dokl. Earth Sci.* **2017**, *473*, 363–366. [[CrossRef](#)]
84. Sorokin, A.A.; Ovchinnikov, R.O.; Kudryashev, N.M.; Kotov, A.B.; Kovach, V.P. Two stages of Neoproterozoic magmatism in the evolution of the Bureya continental massif of the Central Asian Fold Belt. *Russ. Geol. Geophys.* **2017**, *58*, 1171–1187. [[CrossRef](#)]
85. Berdnikov, N.V.; Nevstruev, V.G.; Kepezhinskas, P.K.; Didenko, A.N. The Taragai peridotite massif as an explosive pipe in the western Bureya terrane (Southern Far East of Russia). *Dokl. Earth Sci.* **2023**, *512*, 85–91. [[CrossRef](#)]
86. Kotov, A.B.; Velikoslavinskii, S.D.; Sorokin, A.A.; Kotova, L.N.; Sorokin, A.P.; Larin, A.M.; Kovach, V.P.; Zagornaya, N.Y.; Kurguzova, A.V. Age of the Amur Group of the Bureya-Jiamusi superterrane in the Central Asian Fold Belt: Sm-Nd isotope evidence. *Dokl. Earth Sci.* **2009**, *429*, 1245–1248. [[CrossRef](#)]
87. Park, C.F. A magnetite “flow” in Northern Chile. *Econ. Geol.* **1961**, *56*, 431–436. [[CrossRef](#)]
88. Henriquez, F.; Martin, R.F. Crystal-growth textures in magnetite flows and feeder dikes, El Laco, Chile. *Can. Mineral.* **1978**, *16*, 581–589.
89. Frutos, J.; Oyarzun, J.; Shiga, Y.; Alfaro, G. The El Laco magnetite lava flow deposits in Northern Chile: An up-to-date review and new data. In *Stratabound Ore Deposits in the Andes*; Fontboté, L., Amstutz, G.C., Cardozo, M., Cedillo, E., Frutos, J., Eds.; Special Publication No. 8 of the Society for Geology Applied to Mineral Deposits; Springer: Berlin/Heidelberg, Germany, 1990; pp. 681–690.
90. Yarmolyuk, V.V.; Kudryashova, E.A.; Kozlovsky, A.M.; Lebedev, V.A.; Savatenkov, V.M. Late Mesozoic-Cenozoic intraplate magmatism in Central Asia and its relation with mantle diapirism: Evidence from the South Khangai volcanic region, Mongolia. *J. Asian Earth Sci.* **2015**, *111*, 604–623. [[CrossRef](#)]
91. Tanaka, T.; Togashi, S.; Kamioka, H.; Amakawa, H.; Kagami, H.; Hamamoto, T.; Yuhara, M.; Orihashi, Y.; Yoneda, S.; Shimizu, H.; et al. JNdi-1: A neodymium isotopic reference in consistency with LaJolla neodymium. *Chem. Geol.* **2000**, *168*, 279–281. [[CrossRef](#)]
92. Moore, L.J.; Murphy, T.J.; Barnes, I.L.; Paulsen, P.J. Absolute isotopic abundance ratios and atomic weight of a reference sample of strontium. *J. Res. Natl. Bur. Stand.* **1982**, *87*, 1. [[CrossRef](#)]
93. Whitney, D.L.; Evans, B.W. Abbreviations for names of rock-forming minerals. *Am. Mineral.* **2010**, *95*, 185–187. [[CrossRef](#)]
94. Giordano, G.; Cas, R.A.F. Classification of ignimbrites and their eruptions. *Earth-Sci. Rev.* **2021**, *220*, 103697. [[CrossRef](#)]
95. Shackleton, J.M.; Spry, P.G.; Bateman, R. Telluride mineralogy of the Golden Mile deposit, Kalgoorlie, Western Australia. *Can. Mineral.* **2003**, *41*, 1503–1524. [[CrossRef](#)]
96. Pals, D.; Spry, P. Telluride mineralogy of the low-sulfidation epithermal Emperor gold deposit, Vatukoula, Fiji. *Mineral. Petrol.* **2003**, *79*, 285–307. [[CrossRef](#)]
97. Vikent’eva, O.; Prokofiev, V.; Borovikov, A.; Kryazhev, S.; Groznova, E.; Pritchi, M.; Vikentyev, A.; Bortnikov, N. Contrasting fluids in the Svetlinsk gold-telluride hydrothermal system, South Urals. *Minerals* **2020**, *10*, 37. [[CrossRef](#)]
98. Tolstykh, N.; Vymazalová, A.; Tuhy, M.; Shapovalova, M. Conditions of formation of Au-Se-Te mineralization in the Gaching ore occurrence (Maletoyvayam ore field), Kamchatka, Russia. *Min. Mag.* **2018**, *82*, 649–674. [[CrossRef](#)]
99. Kepezhinskas, P.K.; Berdnikov, N.V.; Krutikova, V.O.; Kepezhinskas, N.P.; Astapov, I.A.; Kirichenko, E.A. Silver mineralization in deep magmatogenic systems of ancient island arcs: The Ildeus ultrabasic massif, Stanovoy mobile belt (Russian Far East). *Russ. J. Pac. Geol.* **2023**, *17*, 322–349. [[CrossRef](#)]
100. Palma, G.; Barra, F.; Reich, M.; Simon, A.C.; Romero, R. A review of magnetite geochemistry of Chilean iron oxide-apatite (IOA) deposits and its implications for ore-forming processes. *Ore Geol. Rev.* **2020**, *126*, 103748. [[CrossRef](#)]
101. Berdnikov, N.; Kepezhinskas, P.; Krutikova, V.; Kozhemyako, N.; Konovalova, N. Cu-Ag-Au microspherules in igneous rocks: Morphology, composition, diagnostic criteria and possible origin. *Minerals* **2023**, *13*, 819. [[CrossRef](#)]
102. Kepezhinskas, P.; Berdnikov, N.; Konovalova, N.; Kepezhinskas, N.; Krutikova, V.; Kirichenko, E. Native metals and alloys in trachytes and shoshonite from the continental United States and high-K dacite from the Bolivian Andes: Magmatic origins of ore metals in convergent and within-plate tectonic settings. *Russ. J. Pac. Geol.* **2022**, *16*, 405–426. [[CrossRef](#)]
103. Kepezhinskas, P.; Berdnikov, N.; Kepezhinskas, N.; Konovalova, N.; Krutikova, V.; Astapov, I. Nature of Paleozoic basement of the Catalan Coastal Ranges (Spain) and tectonic setting of the Priorat DOQ wine terroir: Evidence from volcanic and sedimentary rocks. *Geosciences* **2023**, *13*, 31. [[CrossRef](#)]
104. Kepezhinskas, P.; Berdnikov, N.; Kepezhinskas, N.; Krutikova, V.; Astapov, I. Magmatic-hydrothermal transport of metals at arc plutonic roots: Insights from the Ildeus mafic-ultramafic complex, Stanovoy Suture Zone (Russian Far East). *Minerals* **2023**, *13*, 878. [[CrossRef](#)]
105. Le Bas, M.J.; Le Maitre, R.W.; Streckeisen, A.; Zanettin, B. A chemical classification of volcanic rocks based on the total alkali-silica diagram. *J. Petrol.* **1986**, *27*, 745–750. [[CrossRef](#)]
106. Peccerillo, A.; Taylor, S.R. Geochemistry of Eocene calc-alkaline volcanic rocks from the Kastamonu area, Northern Turkey. *Contrib. Mineral. Petrol.* **1976**, *58*, 63–81. [[CrossRef](#)]

107. McDonough, W.F.; Sun, S.-S. The composition of the Earth. *Chem. Geol.* **1995**, *120*, 223–253. [[CrossRef](#)]
108. Rollinson, H. *Using Geochemical Data: Evaluation, Presentation, Interpretation*, 1st ed.; Longman Scientific and Technical: London, UK, 1993; pp. 1–352.
109. White, W.M. *Geochemistry*, 2nd ed.; Wiley-Blackwell: Hoboken, NJ, USA, 2020; pp. 1–960.
110. Tornos, F.; Hanchar, J.M.; Steele-MacInnis, M.; Crespo, E.; Kamenetsky, V.S.; Casquet, C. Formation of magnetite-(apatite) systems by crystallizing ultrabasic iron-rich melts and slag separation. *Mineral. Depos.* **2023**, 1–37. [[CrossRef](#)]
111. Sorokin, A.A.; Kotov, A.B.; Smirnova, Y.N.; Sal'nikova, E.B.; Plotkina, Y.V.; Yakovleva, S.Z. Age of terrigenous deposits of the Khingan Group in the Lesser Khingan terrane in the eastern part of the Central Asian fold belt. *Dokl. Earth Sci.* **2016**, *471*, 1126–1130. [[CrossRef](#)]
112. Bau, M. Rare-earth element mobility during hydrothermal and metamorphic fluid rocks interaction and the significance of the oxidation-state of europium. *Chem. Geol.* **1991**, *93*, 219–230. [[CrossRef](#)]
113. Mills, R.A.; Elderfield, H. Rare earth element geochemistry of hydrothermal deposits from the active TAG mound, 26°N, Mid-Atlantic Ridge. *Geochim. Cosmochim. Acta* **1995**, *59*, 3511–3524. [[CrossRef](#)]
114. Douville, E.; Bienvenu, P.; Charlou, J.L.; Donval, J.P.; Fouquet, Y.; Appriou, P.; Gamo, T. Yttrium and rare earth elements in fluids from various deep-sea hydrothermal systems. *Geochim. Cosmochim. Acta* **1999**, *63*, 627–643. [[CrossRef](#)]
115. Bau, M.; Schmidt, K.; Koschinsky, A.; Hein, J.; Kuhn, T.; Usui, A. Discriminating between different genetic types of marine ferro-manganese crusts and nodules based on rare earth elements and yttrium. *Chem. Geol.* **2014**, *381*, 1–9. [[CrossRef](#)]
116. Madondo, J.; Canet, C.; González-Partida, E.; Núñez-Useche, F.; Rodrigue-Díaz, A.A.; Rajabi, A.; Colás, V.; Bignon, L.; Vafeas, N.A. Geochemical evidence for a multi-source origin of manganese in the Montaña de Manganeso deposit, central Mexico. *Geochemistry* **2021**, *81*, 125789. [[CrossRef](#)]
117. Schijf, J.; Byrne, R.H. Speciation of yttrium and the rare earth elements in seawater: Review of a 20-year analytical journey. *Chem. Geol.* **2021**, *584*, 120479. [[CrossRef](#)]
118. Zhang, K.; Shields, G.A. Sedimentary Ce anomalies: Secular change and implications for paleoenvironmental evolution. *Earth-Sci. Rev.* **2022**, *229*, 104015. [[CrossRef](#)]
119. Kraemer, D.; Tepe, N.; Pourret, O.; Bau, M. Negative cerium anomalies in manganese (hydr)oxide precipitates due to cerium oxidation in the presence of dissolved siderophores. *Geochim. Cosmochim. Acta* **2017**, *196*, 197–208. [[CrossRef](#)]
120. Yurchenko, Y.Y.; Goltsyn, N.A.; Shupilko, E.V.; Zmievsky, Y.P.; Rasskazov, S.Y.; Anokhina, Z.V. New Isotopic-Geochemical Data on the Age and Composition of Mesozoic Volcanic Complexes of the Lesser Khingan (Jewish Autonomous Region, Far East). In *Tectonics, Deep Structure and Metallogeny of the Eastern Asia, Proceedings of the X Kosygin Conference, Khabarovsk, Russia, 10–12 September 2019*; ITIG: Khabarovsk, Russia, 2019; pp. 121–125. (In Russian)
121. Zhang, C.; Wang, E.; Bi, Z.; Han, R.; Shao, J.; Liu, B.; Chen, J.; Zeng, N. Geochronology and isotope geochemistry studies of an epithermal gold deposit in the northern Lesser Khingan Range, NE China: The Gaosongshan example. *Ore Geol. Rev.* **2019**, *105*, 356–374. [[CrossRef](#)]
122. Zhao, Z.-H.; Sun, J.-G.; Li, G.-H.; Xu, W.-X.; Lu, C.-L.; Gup, Y.; Ren, L.; Hu, Z.-X. Age of the Yongxin Au deposit in the Lesser Xing'an Range: Implications for an Early Cretaceous geodynamic setting for gold mineralization in the NE China. *Geol. J.* **2019**, *54*, 2525–2544. [[CrossRef](#)]
123. Li, G.; Sun, F.; Sun, Y.; Yu, R. Zircon U-Pb geochronology, geochemistry, and Hf isotopic compositions of the trachyandesite in the Dong'an Au deposit, Lesser Xing'an Range, northeastern China. *Geosci. J.* **2021**, *25*, 849–862. [[CrossRef](#)]
124. Didenko, A.N.; Khanchuk, A.I. Change in the geodynamic settings in the Pacific-Eurasia transition zone at the end of the Early Cretaceous. *Dokl. Earth Sci.* **2019**, *487*, 873–876. [[CrossRef](#)]
125. Khanchuk, A.I.; Grebennikov, A.V.; Ivanov, V.V. Albian-Cenomanian orogenic belt and igneous province of Pacific Asia. *Russ. J. Pac. Geol.* **2019**, *13*, 187–219. [[CrossRef](#)]
126. Wang, F.; Xu, W.-L.; Xing, K.-C.; Tang, J.; Wang, Z.-W.; Sun, C.-Y.; Wu, W. Temporal changes in the subduction of the Paleo-Paific plate beneath Eurasia during the late Mesozoic: Geochronological and geochemical evidence from Cretaceous volcanic rocks in eastern NE China. *Lithos* **2019**, 326–327, 415–434. [[CrossRef](#)]
127. Wu, J.; Lin, Y.-A.; Flament, N.; Wu, J.T.-J.; Liu, Y. Northwest Pacific-Izanagi plate tectonics since Cretaceous times from western Pacific mantle structure. *Earth Planet. Sci. Lett.* **2022**, *583*, 117445. [[CrossRef](#)]
128. Yang, F.; Xue, F.; Jepson, G.; Zhang, L. Editorial: (Paleo-) Pacific plate subduction tectonics and related magmatism and mineralization. *Front. Earth Sci.* **2023**, *11*, 1248758. [[CrossRef](#)]
129. Dickinson, W.R.; Hatherton, T. Andesitic volcanism and seismicity around the Pacific. *Science* **1967**, *157*, 801–803. [[CrossRef](#)] [[PubMed](#)]
130. Jakes, P.; White, A.J.R. Major and trace element abundances in volcanic rocks of orogenic areas. *Geol. Soc. Am. Bull.* **1972**, *82*, 323–344.
131. Miyashiro, A. Volcanic rock series in island arcs and active continental margins. *Am. J. Sci.* **1974**, *274*, 321–355. [[CrossRef](#)]
132. Morrison, G.W. Characteristics and tectonic setting of the shoshonite rock association. *Lithos* **1980**, *13*, 97–108. [[CrossRef](#)]
133. Kay, S.M.; Kay, R.W.; Citron, G.P. Tectonic controls of Aleutian arc tholeiitic and calc-alkaline magmatism. *J. Geophys. Res.* **1982**, *87*, 4051–4072. [[CrossRef](#)]
134. Kepezhinskis, P. Diverse shoshonite magma series in the Kamchatka Arc: Relationships between intra-arc extension and composition of alkaline magmas. *Geol. Soc. Lond. Spec. Publ.* **1994**, *81*, 249–264. [[CrossRef](#)]

135. Stern, R.J. Subduction zones. *Rev. Geophys.* **2002**, *40*, 1–38. [[CrossRef](#)]
136. Kepezhinskas, P.; McDermott, F.; Defant, M.J.; Hochstaedter, A.; Drummond, M.S.; Hawkesworth, C.J.; Koloskov, A.; Maury, R.C.; Bellon, H. Trace element and Sr-Nd-Pb isotopic constraints on a three-component model of Kamchatka Arc petrogenesis. *Geochim. Cosmochim. Acta* **1997**, *61*, 577–600. [[CrossRef](#)]
137. Wang, Z.; Lee, S.-W.; Catalano, J.G.; Iezama-Pacheco, J.S.; Bargar, J.R.; Tebo, B.M.; Giammar, D.E. Adsorption of uranium (VI) to manganese oxides: X-ray absorption spectrometry and surface complexation modeling. *Environ. Sci. Technol.* **2013**, *47*, 850–858. [[CrossRef](#)]
138. Gultekin, A.H.; Balci, N. Mineralogy, geochemistry and fluid inclusion data from the Tumanpinari volcanic rock-hosted Fe-Mn-Ba deposit, Balikesir-Dursunbey, Turkey. *Minerals* **2016**, *6*, 120. [[CrossRef](#)]
139. Xing, Y.; Mei, Y.; Etschmann, B.; Liu, W.; Brugger, J. Uranium transport in F-Cl-bearing fluids and hydrothermal upgrading of U-Cu ores in IOCG deposits. *Geofluids* **2018**, *2018*, 6835346. [[CrossRef](#)]
140. Jiménez-Arroyo, A.; Gabitov, R.; Migdisov, A.; Lui, J.; Strzelecki, A.; Zhao, X.; Guo, X.; Paul, V.; Misna, T.; Perez-Huerta, A.; et al. Uranium uptake by phosphate minerals at hydrothermal conditions. *Chem. Geol.* **2023**, *634*, 121581. [[CrossRef](#)]
141. Kepezhinskas, N.; Kamenov, G.D.; Foster, D.A.; Kepezhinskas, P. Petrology and geochemistry of alkaline basalts and gabbroic xenoliths from Utila Island (Bay Islands, Honduras): Insights into back-arc processes in the Central American Volcanic Arc. *Lithos* **2020**, *352–353*, 105306. [[CrossRef](#)]
142. Kepezhinskas, P.; Berdnikov, N.; Kepezhinskas, N.; Konovalova, N. Adakites, high-Nb basalts and copper-gold deposits in magmatic arcs and collisional orogens: An overview. *Geosciences* **2022**, *12*, 29. [[CrossRef](#)]
143. Ben Othman, D.; White, W.M.; Patchett, J. The geochemistry of marine sediments, island arc magma genesis, and crust-mantle recycling. *Earth Planet. Sci. Lett.* **1989**, *94*, 1–21. [[CrossRef](#)]
144. Sasim, S.A.; Dril, S.I.; Travin, A.V.; Vladimirova, T.A.; Gerasimov, N.S.; Noskova, Y.V. Shoshonite-latitude series of the Eastern Transbaikalia: ⁴⁰Ar/³⁹Ar age, geochemistry, and Sr-Nd isotope composition of rocks from the Akatui volcano-plutonic association of the Aleksandrovskii Zavod depression. *Russ. Geol. Geophys.* **2016**, *57*, 756–772. [[CrossRef](#)]
145. Jahn, B.-M. The Central Asian Orogenic Belt and the growth of the continental crust in the Phanerozoic. *Geol. Soc. Lond. Spec. Publ.* **2004**, *226*, 73–100. [[CrossRef](#)]
146. Luan, J.-P.; Wang, F.; Xu, W.-L.; Ge, W.-C.; Sorokin, A.A.; Wang, Z.-W.; Guo, P. Provenance, age, and tectonic implications of Neoproterozoic strata in the Jiamusi Massif: Evidence from U-Pb ages and Hf isotope compositions of detrital and magmatic zircons. *Precambrian Res.* **2017**, *297*, 19–32. [[CrossRef](#)]
147. Kepezhinskas, K.B. Structural-metamorphic evolution of Late Proterozoic ophiolites and Precambrian basement in the Central Asian foldbelt of Mongolia. *Precambrian Res.* **1986**, *33*, 209–223. [[CrossRef](#)]
148. Safonova, I. Juvenile versus recycled crust in the Central Asian Orogenic Belt: Implications from ocean plate stratigraphy, blueschist belts and intra-oceanic arcs. *Gondwana Res.* **2017**, *47*, 6–27. [[CrossRef](#)]
149. Wu, F.-Y.; Jahn, B.-M.; Wilde, S.; Sun, D.Y. Phanerozoic continental crustal growth: Sr-Nd isotopic evidence from the granites in northeastern China. *Tectonophysics* **2000**, *328*, 87–113. [[CrossRef](#)]
150. Yang, H.; Ge, W.-C.; Santosh, M.; Ji, Z.; Dong, Y.; Jing, Y.; Wu, H.-R. The role of continental fragments in the formation of intra-oceanic arcs: Constraints from Sr-Nd-Hf-O isotopes of gabbro from the Jiamusi Block, NE China. *Gondwana Res.* **2022**, *103*, 297–313. [[CrossRef](#)]
151. Long, X.-Y.; Tang, J.; Xu, W.-L.; Sun, C.-Y.; Luan, J.-P.; Guo, P. A crustal growth model for the eastern Central Asian Orogenic Belt: Constraints from granulites in the Songnen Massif and Duobaoshan terrane. *Gondwana Res.* **2022**, *107*, 325–338. [[CrossRef](#)]
152. Zhao, L.; Guo, F.; Fan, W.; Huang, M. Roles of subducted pelagic and terrigenous sediments in early Jurassic mafic magmatism in NE China: Constraints on the architecture of paleo-Pacific subduction zone. *J. Geophys. Res. Solid Earth* **2019**, *124*, 2525–2550. [[CrossRef](#)]
153. Sun, C.; Dasgupta, R. Slab-mantle interaction, carbon transport, and kimberlite generation in the deep upper mantle. *Earth Planet. Sci. Lett.* **2019**, *506*, 38–52. [[CrossRef](#)]
154. Plank, T.; Manning, C.E. Subducting carbon. *Nature* **2019**, *574*, 343–352. [[CrossRef](#)]
155. Wu, W.; Yang, J.; Wirth, R.; Zheng, J.; Lian, D.; Qiu, T.; Milushi, I. Carbon and nitrogen isotopes and mineral inclusions in diamonds from chromitites of the Mirdita ophiolite (Albania) demonstrate recycling of oceanic crust into the mantle. *Am. Mineral.* **2019**, *104*, 485–500. [[CrossRef](#)]
156. Dai, L.-Q.; Zhao, K.; Zhao, Z.-F.; Zheng, Y.-F.; Fang, W.; Zha, X.-P.; An, Y.-J. Magnesium-carbon isotopes trace carbon recycling in continental subduction zone. *Lithos* **2020**, *376–377*, 105774. [[CrossRef](#)]
157. Li, K.; Li, L.; Aubaud, C.; Muehlenbachs, K. Efficient carbon recycling at the Central-Northern Lesser Antilles Arc: Implications to deep carbon recycling in global subduction zones. *Geophys. Res. Lett.* **2020**, *47*, e2020GL086950. [[CrossRef](#)]
158. Schidlowski, M. Carbon isotopes as biogeochemical recorders of life over 3.8 Ga of Earth history: Evolution of a concept. *Precambrian Res.* **2001**, *106*, 117–134. [[CrossRef](#)]
159. Schopf, J.W.; Kudryavtsev, A.B. Biogenicity of Earth's Earliest Fossils. In *Evolution of Archean Crust and Early Life*; Dilek, Y., Furnes, H., Eds.; Springer: Dordrecht, The Netherlands, 2014; Volume 7, pp. 333–349.
160. Garcia, A.K.; Cavanaugh, C.M.; Kacar, B. The curious consistency of carbon biosignatures over billions of years of Earth-life coevolution. *ISME J.* **2021**, *15*, 2183–2194. [[CrossRef](#)] [[PubMed](#)]

161. Smart, K.A.; Chacko, T.; Stachel, T.; Muehlenbachs, K.; Stern, R.A.; Heaman, L.M. Diamond growth from oxidized carbon sources beneath the Northern Slave Craton, Canada: $\delta^{13}\text{C}$ -N study of eclogite-hosted diamonds from the Jericho kimberlite. *Geochim. Cosmochim. Acta* **2011**, *75*, 6027–6047. [[CrossRef](#)]
162. Walter, M.J.; Kohn, S.C.; Araujo, D.; Bulanova, G.P.; Smith, C.B.; Gaillou, E.; Wang, J.; Steele, A.; Shirey, S.B. Deep mantle cycling of oceanic crust: Evidence from diamonds and their mineral inclusions. *Science* **2011**, *334*, 54–57. [[CrossRef](#)] [[PubMed](#)]
163. Mathez, E.A.; Fogel, R.A.; Hutcheon, I.D.; Marshintsev, V.K. Carbon isotopic composition and origin of SiC from kimberlites of Yakutia, Russia. *Geochim. Cosmochim. Acta* **1995**, *59*, 781–791. [[CrossRef](#)]
164. Trumbull, R.B.; Yang, J.-S.; Robinson, P.T.; di Pierro, S.; Vennemann, T.; Wiedenbeck, M. The carbon isotope composition of natural SiC (moissanite) from the Earth's mantle. New discoveries from ophiolites. *Lithos* **2009**, *113*, 612–620. [[CrossRef](#)]
165. Kepezhinskas, P.; Kepezhinskas, N. ^{13}C -depleted moissanites in subduction-related rocks: Tracers of slab fluids in the Earth's mantle and a new diamond exploration tool. In *E3S Web Conferences*; EDP Sciences: Les Ulis, France, 2019; Volume 98, p. 08009. [[CrossRef](#)]
166. Suess, E.; Whiticar, M.J. Methane-derived CO_2 in pore fluids expelled from the Oregon subduction zone. *Paleogeogr. Palaeoclimatol. Paleocol.* **1989**, *71*, 119–136. [[CrossRef](#)]
167. Yamaguchi, A.; Ujiie, K.; Nakai, S.; Kimura, G. Sources and physicochemical characteristics of fluids along a subduction-zone megathrust: A geochemical approach using syn-tectonic mineral veins in the Mugi mélange, Shimanto accretionary complex. *Geochem. Geophys. Geosyst.* **2012**, *13*. [[CrossRef](#)]
168. Barry, P.H.; Nakagawa, M.; Giovanelli, D.; de Moor, J.M.; Schrenk, M.; Seltzer, A.M.; Manini, E.; Fattorini, D.; dii Carlo, M.; Regoli, F.; et al. Helium, inorganic and organic carbon isotopes of fluids and gases across the Costa Rica convergent margin. *Sci. Data* **2019**, *6*, 284. [[CrossRef](#)] [[PubMed](#)]
169. Barry, P.H.; De Moor, J.M.; Chiodi, A.; Aguilera, F.; Hudak, M.R.; Bekaert, D.V.; Turner, S.J.; Curtice, J.; Seltzer, A.M.; Jessen, G.L.; et al. The helium and carbon isotope characteristics of the Andean convergent margin. *Front. Earth Sci.* **2022**, *13*, 897267. [[CrossRef](#)]
170. Lopez, T.; Fischer, T.P.; Plank, T.; Malinverno, A.; Rizzo, A.L.; Rasmussen, D.J.; Cottrell, E.; Werner, C.; Kern, C.; Bergfeld, D.; et al. Tracking carbon from subduction to outgassing along the Aleutian-Alaska volcanic arc. *Sci. Adv.* **2023**, *9*, 26. [[CrossRef](#)]
171. Peter, J.M.; Shanks III, W.C. sulfur, carbon, and oxygen isotope variations in submarine hydrothermal deposits of Guaymas Basin, Gulf of California, USA. *Geochim. Cosmochim. Acta* **1992**, *56*, 2025–2040. [[CrossRef](#)]
172. Reeves, E.P.; Seewald, J.S.; Saccocia, P.; Bach, W.; Craddock, P.R.; Shanks, W.C.; Sylva, S.P.; Walsh, E.; Pichler, T.; Rosner, M. Geochemistry of hydrothermal fluids from the PACMANUS Northeast Pual and Vienna Woods hydrothermal fields, Manus Basin, Papua New Guinea. *Geochim. Cosmochim. Acta* **2011**, *75*, 1088–1123. [[CrossRef](#)]
173. Wen, H.-Y.; Sano, Y.; Takahata, N.; Tomonaga, Y.; Ishida, A.; Tanaka, K.; Kagoshima, T.; Shrai, K.; Ishibashi, J.-I.; Yokose, H.; et al. Helium and methane sources and fluxes of shallow submarine hydrothermal plumes near the Tokara Islands, Southern Japan. *Sci. Rep.* **2016**, *6*, 34216. [[CrossRef](#)] [[PubMed](#)]
174. Neuholz, R.; Kleint, C.; Schnetger, B.; Koschinsky, A.; Laan, P.; Middag, R.; Sander, S.; Thal, J.; Türke, A.; Walter, M.; et al. Submarine hydrothermal discharge and fluxes of dissolved Fe and Mn, and He isotopes at Brothers Volcano based on radium isotopes. *Minerals* **2020**, *10*, 969. [[CrossRef](#)]
175. Golozubov, V.V.; Khanchuk, A.I. The Heilongjiang complex as a fragment of a Jurassic accretionary wedge in the tectonic windows of the overlying plate: A flat slab subduction model. *Russ. J. Pac. Geol.* **2021**, *15*, 279–292. [[CrossRef](#)]
176. Didenko, A.N.; Nosyrev, M.Y. Reflection of paleo- and modern geodynamic processes in the deep structure of the Sikhote-Alin orogenic belt. In: *Geologic Processes in the Lithospheric Plates Subduction, Collision, and Plate Environments*. In Proceedings of the IV Russian Scientific Conference with Foreign Participants, Vladivostok, Russia, 17–23 September 2018; 326p. (In Russian)

Disclaimer/Publisher's Note: The statements, opinions and data contained in all publications are solely those of the individual author(s) and contributor(s) and not of MDPI and/or the editor(s). MDPI and/or the editor(s) disclaim responsibility for any injury to people or property resulting from any ideas, methods, instructions or products referred to in the content.